Mechanical Systems and Signal Processing 249 (2026) 114054

Contents lists available at ScienceDirect

Mechanical Systems and Signal Processing

journal homepage: www.elsevier.com/locate/ymssp

Full Length Article

Narrow and third-octave spectra of total flexural vibration and sound power radiation from optical camera measurements

Paolo Gardonio [a,*], Sofia Baldini [a], Domen Gorjup [b], Janko Slavič [b], Roberto Rinaldo [a]

[a] Università Degli Studi di Udine, Dipartimento Politecnico di Ingegneria e Architettura, Italy
[b] University of Ljubljana - Faculty of Mechanical Engineering, Askerceva 6, 1000 Ljubljana, Slovenia

ARTICLE INFO

Keywords:
Sound measurement
Vibration measurement
Narrow band
Third-octave band
Videogrammetry
Multi-view
Frequency triangulation

ABSTRACT

This research presents an optical camera-based method for measuring narrow band and third-octave band spectra of the total flexural vibration and total sound radiation of 2D and 3D structures. The proposed method overcomes key issues inherent in classical vibro-acoustic measurements, such as the requirement of long-duration and full-field measurements and, to some extent, the need of physically masking flanking sources and background noise. Digital image correlation combined with frequency-domain triangulation is employed, which is particularly suited for the derivation of spectral measurements, although classical time-domain triangulation could be employed too. The narrow-band vibration and sound radiation spectra are derived from integral formulations. In particular, the total sound power radiation is derived using the radiation resistance matrix, which can be calculated from numerical quadrature of the boundary integral for the sound radiation. The third-octave band spectra are computed by integration of the narrow band spectra over appropriate frequency-bands. The proposed method is validated for a baffled cylinder model-structure by contrasting the narrow band and third-octave band spectra of the total flexural vibration and total sound power radiation estimated from camera recordings with those obtained from direct measurements taken with a scanning laser vibrometer and a microphones array. The proposed approach offers a valid alternative to traditional vibroacoustic measurements, which does not require expensive laboratory facilities and long lasting and costly measurement campaigns. Furthermore, it can be effectively integrated into laboratory equipment for the offline synthesis and measurement of specific vibroacoustic fields, thus reducing the costs and time of conventional tests on real systems, such as the measurement of a) car tire noise, b) airplane cabin noise caused by the aerodynamic turbulence and the engines, c) room airborne and structure-borne noise produced by household appliances, and d) interior noise transmission through windows and partitions of building.

1. Introduction

The spectral measurement of the total flexural vibration and total sound radiation by structures is of great importance for the analysis of Noise, Vibration and Harshness (NVH) of transportation vehicles (in particular sound transmission/radiation by wall

* Corresponding author.
E-mail address: paolo.gardonio@uniud.it (P. Gardonio).

https://doi.org/10.1016/j.ymssp.2026.114054
Received 9 August 2025; Received in revised form 15 January 2026; Accepted 19 February 2026
Available online 25 February 2026

panels) as well as for the Noise and Vibration (N&V) classification of domestic appliances (normally sound radiation by flexible enclosures and housings) and structural components of buildings (principally sound transmission through partitions and windows) [1,2]. In general, acoustic measurements are implemented either in situ (for example with microphones [2–4], nearfield holography techniques [5,6], sound intensity probes [7,8], acoustic cameras [9–12]) or in large anechoic or reverberant rooms [2,13,14]. Both solutions present a few drawbacks linked to background and flanking disturbances, accuracy and repeatability of the measurement, cost of the equipment and of the infrastructure (for more details see monographs by Bies *et al.* [2] and by Fahy [15]). For these reasons, a new approach based on the reconstruction from full-field camera measurements of the vibration and sound radiation of structures has been recently explored by Gardonio *et. al.* [16–19]. In these early studies, both classical 3D-Point-Tracking (3DPT) (e.g. see Refs. [20–26]) and Digital-Image-Correlation (DIC) (e.g. see Refs. [20,26–36]) were employed to reconstruct the vibration field and thus the radiated sound field.

At present, quite a lot of fundamental research is still in progress for both 3DPT and DIC camera measurement approaches. For instance, in 2024 Pastor-Cintas *et al.* [37] have investigated the effect of temperature on DIC videogrammetry. Also, a review article has been presented in Ref. [38] that covered several techniques for motion magnification of video-based vibration measurements of civil structures. More recently in 2025 Luo *et al.* [39] have proposed a new subpixel motion estimation for camera-based vibration monitoring under complex exogenous conditions. Also, Mastrodicasa *et al.* [34] presented a 3D-DIC modal analysis approach for aircraft structures, which relies on low-speed cameras. Xiong *et al.* [40] proposed a method that incorporates an optical field correction model into the intensity-based optical flow framework to enhance vibration measurements with low illumination. Luo *et al.* [41] presented an adaptive wavelength approach to enhance Phase Motion Estimation (PME) techniques based on optical camera acquisitions. Finally, Leclère *et al.* [42] have produced a comprehensive overview of a competition that was organised in 2023 to demonstrate the possibility of diagnosing a bearing operating at a variable rotation speed using high-speed video data only. In general, both 3DPT and DIC methods rely on stereo image acquisitions taken with two synchronized cameras [29] and classical triangulation techniques to reconstruct the vibration displacements at a grid of target points of the structure at hand [43–45]. As discussed in Hartley and Zisserman [46], the accuracy of the measurement can be significantly improved by employing multiple, i.e. more than 2, synchronized cameras. Nevertheless, stereo and multi-camera video acquisitions are rather delicate to perform, particularly because they rely on perfect synchronization of two or more cameras [47] and because they require an accurate calibration process [46–50]. To avoid the synchronization problem, and to reduce the complexity and cost of the measurement procedure, the implementation of multi-view triangulation from single camera acquisitions has been investigated during the past decade [51–61]. In particular, Gorjup *et. al.* [62] have proposed a frequency-domain triangulation technique, which has proven quite effective for spectral measurements of vibrations. Besides, in Ref. [56], they have developed a measurement approach where still DSLR (Digital Single-Lens Reflex camera) images of a vibrating objects are used with modulating illumination to measure spectral operating deflection shape images from multiple viewpoints.

The principal advantage of the vibro-acoustic measurement approach proposed in Refs. [16–19] is given by the fact that it does not require specific acoustic facilities and measurement setups to mask the effect of external noise and flanking sources, unless they are strong enough to modify the vibration of the radiating sample. Moreover, it relies on full field acquisitions taken over rather short time windows, so that the measurement is not influenced by variations of the measurement conditions (e.g. temperature, imposed tensioning, etc.). The method can be employed for spectral measurements of the sound radiation by 2D and 3D thin structures (such as beams, flat and curved panels, closed shells, boxes built from flat panels, etc.) and by 3D mechanical parts (e.g. bulky mechanical components and whole machines, etc.). Also, it can be implemented both in-situ (buildings, production plants, air and surface vehicles, etc) or in laboratory rooms, which nevertheless do not necessarily need to comply with typical anechoic or reverberation standards [2,13,14]. Finally, it can be suitably used to isolate the sound radiation of a specific section of the vibrating structure or machinery. Beside these advantages, sound radiation measurements with cameras present a few drawbacks that should be taken into consideration such as, for example, the cost of high-speed, high-resolution camera systems, the need of advanced computing infrastructure and specialized software. Also, it is likely that the approach will suffer from intrinsic limitations for the detection of low amplitude vibrations at high frequencies. Finally, it is specifically suited for the reconstruction of structure-borne noise radiation and cannot be used to detect air-borne sound radiation. At present it is rather difficult to make a cost-benefit analysis for this new measurement approach, principally because off the shelf cameras, computers and software have been used in the early experiments. As often happens in practice, it will all depend on whether the technology has access to low-cost high-speed and high-resolution cameras and high-performance computing machines as well as the availability of open-source software for the image processing and the sound radiation calculations [63]. Nevertheless, at present, there is quite a lot of interest on the possibility of measuring both vibration and sound radiation spectra from full field camera recordings taken on flexible structures and mechanical components or machines.

In this context, a novel, self-contained, formulation is presented here for the derivation of narrow band and third-octave band spectra of the total flexural kinetic energy and total sound power radiation of distributed structures from multi-view video acquisitions taken with a single camera. The two spectral functions are derived from integrations of the flexural vibration field reconstructed from the camera measurements over the surface of the radiating body. In contrast to classical approaches, the total sound power radiation is derived by collapsing onto the radiation surface itself the far-field surface over which the sound intensity is normally integrated. This has led to consistent matrix formulations for the total flexural kinetic energy and the total sound power radiation, where the latter incorporates a radiation resistance matrix. In this study, both the narrow band and third-octave band spectra of the total flexural vibration and total sound radiation of a baffled cylinder model-structure derived from camera measurements with the proposed formulation are validated against measurements taken with a scanning laser vibrometer and a microphones array respectively. The baffled cylinder research-case has been chosen for two principal reasons. Firstly, because it is a "geometrically-complex" structure with a closed and curved surface whose sound radiation can nevertheless be derived in analytical form. Secondly, because it represents a

"dynamically-rich" structure whose flexural response is characterised by a fast increment of the flexural modal density with frequency [64,65]. Hence, at low frequencies, the spectrum of the total sound power radiation shows well separated resonance peaks, whereas at higher frequencies it displays a spectrum with wider band crests and troughs due to the constructive or destructive overlap of the dynamic responses of multiple modes at each frequency. In practice, for realistic structures and machineries characterised by complex geometries, numerical approaches like the acoustic Boundary Element Method (BEM) and the acoustic Finite Element Method (FEM) should be employed [65].

The article is structured in six Sections including the last one with the conclusions of the study. To start with, Section 2 describes the baffled-cylinder model structure, the camera video recording setup and the vibration and acoustic measurement arrangements used to validate the proposed camera approach for the reconstruction of the flexural vibration and sound radiation of the model structure. Next, Section 3 presents the core formulation for the derivation from camera measurements of the spectra of the total flexural vibration and total sound power radiation of the model-structure. Then, Section 4 presents experimental results where the narrow and third-octave band spectra of the total flexural vibration and total sound radiation derived from the camera measurements are contrasted with those measured with a scanning laser vibrometer and an array of microphones. Finally, Section 5 discusses the extension of the proposed measurement approach to real case structures, which relies on BEM and FEM models. Moreover, it provides detailed analyses of the challenges yet to be addressed before the proposed measurement technique can be implemented on a wide range of structures.

2. General research-case and measurement setups

To provide a general research-case, the thin-walled circular cylinder connected to rigid baffles shown in Fig. 1a has been used as

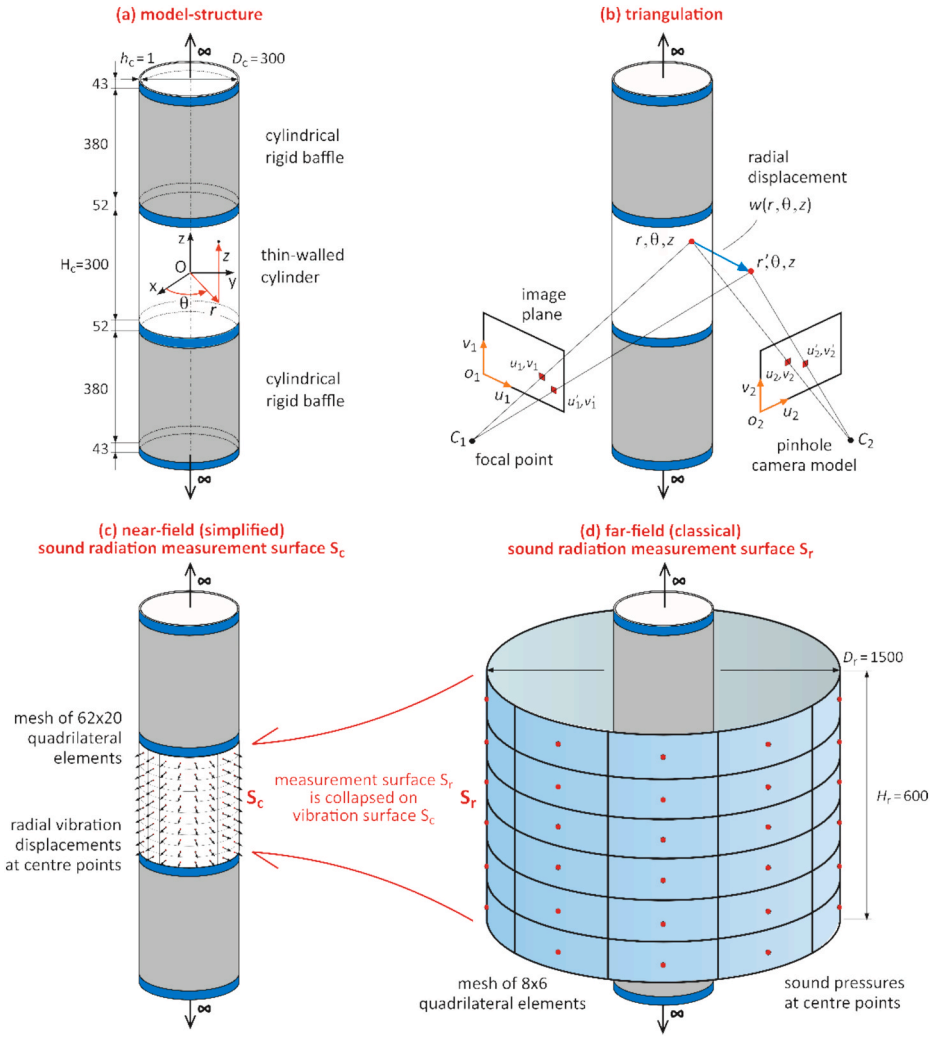

Fig. 1. (a) model structure, (b) triangulation to reconstruct radial displacements, (c) proposed near-field sound radiation measurement surface with 62 × 20 mesh of quadrilateral elements and (d) classical far-field sound radiation measurement surface with 8 × 6 mesh of quadrilateral elements (dimensions in mm).

model-structure. This is one of the few closed shell structures whose sound radiation can be derived from closed-form analytical expressions [66]. For more practical structures, numerical approaches like BEM or FEM should be employed instead [65]. As shown in Fig. 1b, the proposed method is based on the reconstruction of the cylinder radial displacements due to flexural vibrations from triangulation of images acquired from two (or more) viewpoints. More specifically, as depicted in Fig. 1c, the radial displacements are reconstructed at the centres of the regular mesh of $N = 62 \times 20 = 1240$ quadrilateral elements covering the whole surface of the cylinder (20 elements along the length and 62 along the circumference of the cylinder). The total flexural kinetic energy is derived as the summation of the kinetic energies of the quadrilateral elements. Similarly, the total sound radiation is calculated from a discretized form of the Kirchhoff – Helmholtz integral for the sound radiation of flexible bodies into free-field [65–69], which summates the self and mutual radiation effects of the quadrilateral pistons in an infinitely extended rigid cylindrical baffle [65].

Before entering into the details of the mathematical formulations for the reconstruction of the flexural vibration from camera video acquisitions and for the derivation of the spectra of the total flexural response and total sound power radiation, the thin-walled baffled cylinder model-structure employed in this study is first presented below together with the camera setup for the video acquisitions used to reconstruct the spectra of the cylinder total flexural vibration and total sound radiation. The laser vibrometer with a scanning head and the microphone array used to acquire reference spectral measurements are also illustrated.

2.1. Model structure

As shown in Figs. 1a and 2a, the model-structure is made by a thin-walled flexible cylinder, equipped with two heavy baffle extensions characterised by negligible flexural vibrations. The three components are made by thin-walled cylinders of steel with thickness $h_c = 1$mm and inner diameter $D_c = 300$mm and are connected to each other via circular flanges. The bottom flange of the lower baffle is mounted onto a heavy base disk via a turning joint such that, as depicted in the Fig. 2a, the whole assembly can be rotated around the vertical axis. This solution is instrumental to implement both multi-view camera acquisitions of the structure with a fixed camera and multiple vibration and sound pressure measurements with a fixed scanning laser vibrometer and a fixed vertical array of microphones respectively. To have dampened and heavy bodies, the two baffle cylinders were filled with sand. In principle, the two baffles should be infinitely long, but for practical purposes, as shown in Fig. 1a, their lengths have been set to be about 1.6 times of that of the cylinder. In this way, the local acoustic scattering effect near the terminations of the flexible cylinder is preserved such that, in its proximity, the sound radiation field replicates quite accurately that of an idealised cylinder connected to infinitely long baffle extensions. As a result, the total sound power radiation was properly measured in an anechoic room with a microphones array. As can be seen in Fig. 2b, the cylinder was coated with a thin film painted with a speckle pattern necessary for the implementation of DIC videogrammetry [20,26–36]. The cylinder was excited in bending by a radial point force exerted with an electro-magnetic shaker located inside the cylinder itself. The force exerted by the shaker was measured with a load cell mounted at the tip of the stinger used to connect the shaker to the cylinder wall.

2.2. Camera measurement setup

As depicted schematically in Fig. 1b, the reconstruction of the vibration field from camera video recordings is based on triangulation of video-acquisitions taken from different viewpoints (here the cameras are represented with the so-called pinhole model [47,70]). To enhance the accuracy of the measurement, and to cover the whole surface of the cylinder, rather than stereo video acquisitions, multiple acquisitions from an ensemble of $V = 18$ viewpoints were taken. More specifically, as shown in Fig. 3, instead of using 18 fixed cameras that simultaneously recorded images from 18 viewpoints, a single camera solution was adopted, where the camera was kept fixed and acquired a sequence of multi-views while the cylinder was rotated by incremental steps in between

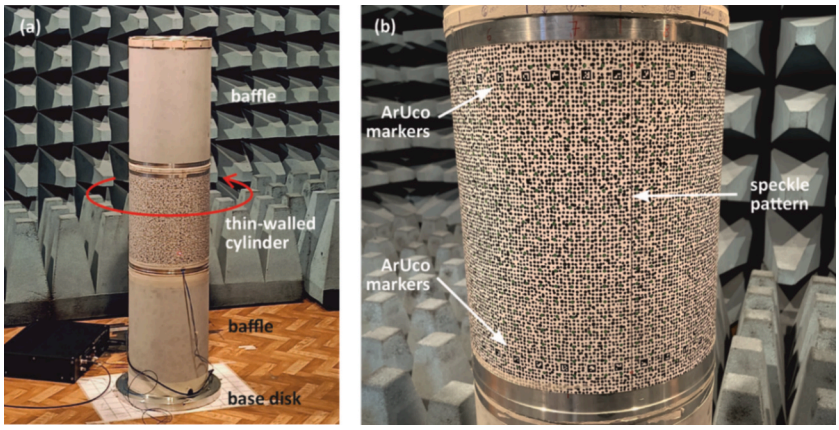

Fig. 2. (a) thin-walled cylinder with two heavy baffles extension mounted on base disk via a turning joint; (b) cylinder coated with a thin film painted with a speckle pattern for the DIC videogrammetry and ArUco markers for the extrinsic camera calibration.

acquisitions. To this end, the vibration field was reconstructed with the frequency-domain triangulation proposed in Refs. [56,62], which, for completeness, is briefly recalled in Section 3.1 below.

Having many viewpoints is not a mere requirement for the measurement of the flexural vibration field of the whole surface of the 3D cylindrical shell. On the contrary, it is also a mean to increase the accuracy of the vibration field reconstruction (e.g. see Ref. [47]). In fact, as the schematic drawing in Fig. 4 visualizes in two-dimensions using the pinhole model for the camera [47,70], if a single view-point were used, then, as depicted in sketch (a), the position of the dot would be restricted on a cone open-surface defined by the two straight lines that pass by the focal point of the camera and the edges of the pixel lightened by the dot. To restrict the localization of the dot to a closed-surface, two view-points are normally used. In this case, as shown in sketch (b), the position of the dot would be limited to the blue area given by the intersection of the two cones. Normally, the position of the dot is set at the centroid of the blue area. If, as depicted in sketch (c), additional view-points were added, then the blue area would be sliced into incrementally smaller blue surfaces such that the position of the dot would be reconstructed with greater accuracy.

Fig. 5 shows the camera setup used in this study. The video acquisitions were taken with a Photron FASTCAM SA-Z high-speed and high-resolution optical camera. The camera acquired 50.000 12-bit monochrome images at 10.000 frames-per-second, with a spatial resolution of 896 $\times$ 896 pixels. Two LED light reflectors were used to lighten the measurement area of the cylinder. A two-stages calibration was performed. Firstly, the intrinsic camera calibration was implemented by taking multiple images of a standard checkerboard that was appropriately displaced and rotated in between acquisitions of the images. Since the optic of the camera was kept fixed during the multi-image acquisitions, this exercise was executed only once and provided the focal length and the optical centre of the camera, which were then incorporated in the so-called intrinsic camera calibration matrix $\mathbf{K}$ [49]. Secondly, the extrinsic camera calibration was performed using the Perspective-n-Point algorithm [71]. The reference images of each multi-view measurement video, taken from the 18 viewpoints selected for the multi-view camera acquisitions, were used in this process. Here, the actual spatial positions of ArUco markers printed on the film coated on the cylinder close to the top and bottom rims (see Figs. 2b and 5c) were combined with their automatically detected projections on the camera image plane for the whole set of 18 viewpoints to give the perspective camera rotation matrices $\mathbf{R}_v$ and translation vectors $\mathbf{t}_v$ for the 18 viewpoints. Overall, the intrinsic and extrinsic camera calibrations provided a fully calibrated multi-view imaging setup, with known perspective camera projection matrices $\mathbf{P}_v$ [46]:

$$\mathbf{P}_v = \mathbf{K}[\mathbf{R}_v|\mathbf{t}_v], \tag{1}$$

where $v = 1, \cdots, V$ with $V = 18$. In this expression, the cameras calibration matrix $\mathbf{K}$ transforms the normalized image coordinates into the image coordinates expressed in pixels (e.g. see Ref. [47] for more details). Also, it provides the camera scaling, which is controlled by the focal length f of the camera.

2.3. Laser vibrometer and microphone array measurement setups

To assess the validity of the proposed measurement approach, the spectra of the cylinder flexural vibration and sound radiation obtained from the camera video acquisitions were contrasted with those measured with a Polytec PSV-500-NB laser vibrometer and an array of PCB 130F20 microphones respectively. More specifically, the laser vibrometer was set to measure the radial velocities of the cylinder at the centres of the 62 $\times$ 20 mesh of quadrilateral elements it had been subdivided into (see Fig. 1c). To this end, as can be seen in Fig. 6b, the thin film with the speckle pattern glued onto the cylinder was augmented with a lattice of green dots that provided a reference for the pointer of the laser vibrometer. Also, as shown in Fig. 6a, the laser was arranged in such a way as to acquire

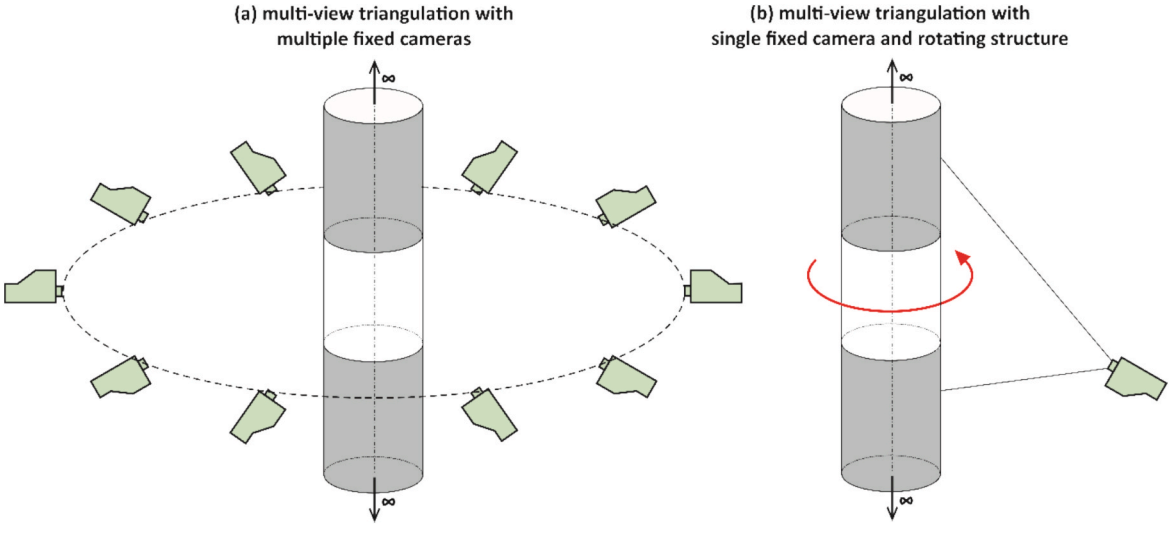

Fig. 3. Multiview camera measurements taken (a) simultaneously on a still cylinder with an ensemble of fixed synchronized cameras and (b) sequentially with a single fixed camera on a cylinder, which is rotated by incremental steps in between recordings.

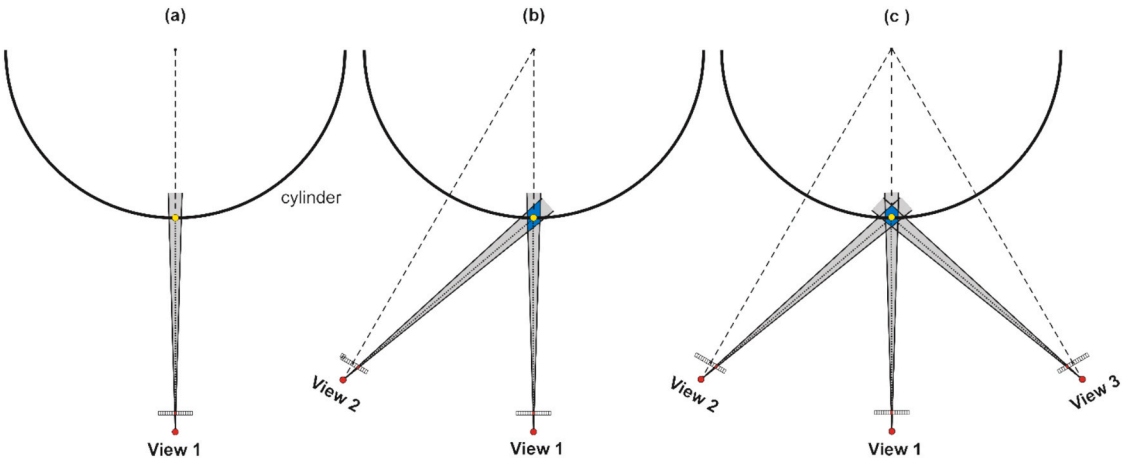

Fig. 4. Localization of a dot from triangulation of camera multi-views. (a) single view locates the dot on a cone open-surface. (b) two views locate the dot on the blue closed-surface given by the intersection of two view-cones. (c) the area of the blue closed-surface is sliced down by the intersections of multiple view-cones. (For interpretation of the references to colour in this figure legend, the reader is referred to the web version of this article.)

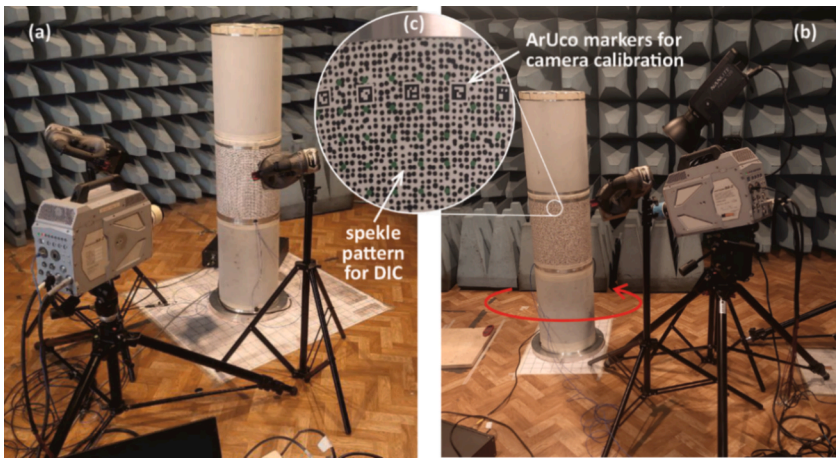

Fig. 5. Camera measurement setup with (a) the FASTCAM SA-Z high-speed and high-resolution monochromatic optical camera and two lights, (b) the baffled cylinder mounted on the heavy base disk via a turning joint, which is coated with (c) a thin film with painted the speckle pattern used for the DIC videogrammetry and the ArUco makers used for the extrinsic camera calibration.

sequentially with the scanner head the vibrations along a vertical line of 18 measurement points. As done with the cameras, to acquire the whole set of 62 lines of points, rather than turning the laser around the cylinder, the cylinder itself was rotated by incremental steps of 6DEG. The laser vibrometer was set to measure mobility Frequency Response Functions (FRFs), given by the ratio of the radial velocity measured at the target points and the radial force exerted by the shaker, which was measured with the load cell fixed at the tip of the stinger. The measured mobility FRFs were then used to reconstruct the spectrum of the total flexural vibration of the cylinder, which was expressed in terms of the total flexural kinetic energy.

The total sound radiation was measured with the vertical array of microphones shown in Fig. 6c. The measurement was carried out according to the ISO 3740:2019 and ISO 3744:2010 guidelines (see Refs. [3,4]) for the estimation of sound radiation in an anechoic room. In general, this measurement is carried out in a semi-anechoic room by placing the tested object on the floor and taking sound pressure measurements on a grid of points lying on a large hemispherical surface where the sound field produced by the radiator can be locally approximated as a plane wave such that the radiated sound power can be derived from measurements of the sound pressure only [2]. Given the peculiar shape of the baffled cylinder radiator considered here, as can be seen in Fig. 6c, the measurement was carried out in a fully anechoic room and the sound pressures were taken on a large cylindrical surface, which was extended over the two baffles. In this way, both the sound radiated directly by the cylinder and the sound scattered by the two baffles were measured appropriately. For the given dimensions of the baffled cylinder and of the whole anechoic room, the measurement cylindrical surface was taken to have a diameter $D_s = 1500$mm and a height $H_s = 600$mm such that it extends over the baffles by $\Delta_H = 150$mm. For practical reasons, the sound pressures were measured on a coarse 8×6 grid of points (8 in circumferential and 6 in axial direction). As

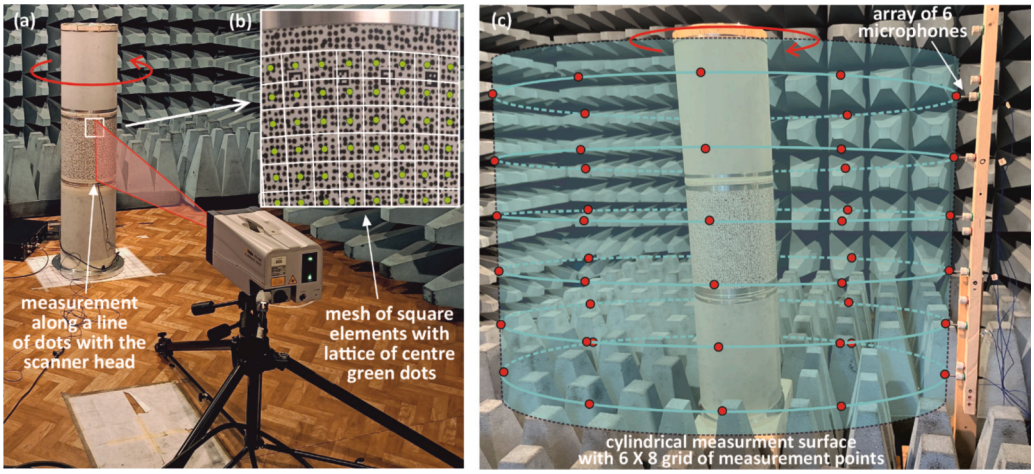

Fig. 6. Vibration and sound radiation measurement setups. (a) Polytec PSV-500-NB Laser vibrometer with a scanner head used to measure the radial velocities at (b) the grid of 62×20 measurement points highlighted by green dots in the film coated on the cylinder (green colour is augmented to better visualise the dots). (c) Array of 6 PCB 130F20 microphones used to measure the sound radiation pressure at a grid of 6×8 red points on the cyan cylindrical measurement surface solid to the cylinder (for both measurements, the laser/microphone-array are kept fixed whereas the cylinder, and thus the cyan measurement surface, are turned sequentially). (For interpretation of the references to colour in this figure legend, the reader is referred to the web version of this article.)

depicted schematically in Fig. 1d, the measurement points were located at the centre of a 8×6 regular mesh of quadrilateral elements. The measurements were taken with the vertical array of 6 microphones shown in Fig. 6c and, as done with the laser vibrometer, the acquisitions were repeated 8 times with 45 (DEG) rotations of the baffled cylinder that produced the 8×6 grid of measurements solid to the cylinder.

3. Flexural vibration and sound radiation spectra from fixed camera multi-view acquisitions

This section introduces the formulations for deriving the spectra of the total flexural vibration and total sound radiation from the multi-view video acquisitions gathered with the fixed camera while the cylinder is rotated in between acquisitions. To allow a full understanding of the method proposed in this article, at first the reconstruction of the vibration field based on the frequency-domain triangulation presented in [56,62] is briefly recalled in Section 3.1. Next, the derivation in terms of compact matrix expressions of the spectra of the total flexural kinetic energy and total sound power radiation is presented in detail in Sections 3.2 and 3.3 respectively. The two formulations are based on integral expressions of the flexural velocity and sound intensity fields over the radiating surface, that is the surface of the flexible cylinder (See Fig. 1c). The sound intensity field is derived directly from the vibration field using the Kirchhoff-Helmholtz (K-H) boundary integral formulation for the sound radiation of flexible structures into free-field [65–69]. For completeness, the alternative formulation where the total sound power radiation is derived from the integral of the sound intensity field over a far-field radiation surface (See Fig. 1d) is also presented. In this case too, the far-field sound intensity is reconstructed using the Kirchhoff-Helmholtz boundary integral. In conclusion Section 3.4 presents the equivalent compact matrix formulae for the spectra of the total flexural kinetic energy and total sound power radiation derived from direct measurements of the vibration field and sound intensity field obtained respectively with the laser vibrometer and the grid of microphone measurements.

The formulations presented in this article are based on time-harmonic functions $g(t)$ (i.e. acoustic/vibration displacements, velocities, forces, pressures), which, in general, are defined in the following complex form:

$$g(t) = \mathrm{Re}\{g(\omega)e^{j\omega t}\}, \tag{2}$$

where, $g(\omega)$ is the complex amplitude, ω is the circular frequency and $j = \sqrt{-1}$. It is important to stress that an $\exp(j\omega t)$ time-dependence has been adopted, which has quite a relevant impact on the expression for the sound radiation generated by the cylinder model structure [72].

3.1. Cylinder flexural vibration from multi-view camera acquisitions

Fig. 1b shows a simplified outline of the triangulation working principle with two cameras, which relies on the pinhole model for the projection of the seen on the image plane of the cameras [47,70]. As depicted in the sketch, when the point highlighted by the red dot is displaced radially from the reference position (r, θ, z) to (r', θ, z), its images in the two cameras move from positions (u_{v1}, v_{v1}) and (u_{v2}, v_{v2}) to positions (u'_{v1}, v'_{v1}) and (u'_{v2}, v'_{v2}) respectively. The pinhole model establishes a relation between the coordinates of the point and the coordinates of its images into the camera plane. For instance, considering the dot at position $\mathbf{x}$, the following matrix

relation can be established for the v-th viewpoint:

$$\mathbf{y}_{\mathrm{v}}(t) = \frac{1}{w_{\mathrm{v}}}\mathbf{P}_{\mathrm{v}}\mathbf{x}(t), \tag{3}$$

Here, $\mathbf{x} = [x, y, z, 1]^{\mathrm{T}}$ is the homogeneous vector that defines the position of the dot with respect to the global Cartesian system of reference $(\mathrm{O}, \mathrm{x}, \mathrm{y}, \mathrm{z})$ solid to the cylinder and $\mathbf{y}_{\mathrm{v}} = [u_{\mathrm{v}}, v_{\mathrm{v}}, 1]^{\mathrm{T}}$ is the homogeneous vector that defines the position of the dot projection into the image plane of the camera for the v-th viewpoint with respect to the local Cartesian systems of reference $(\mathrm{o}, \mathrm{u}, \mathrm{v})$. Moreover, w_{v} is the v-th scale factor and $\mathbf{P}_{\mathrm{v}}$ is the v-th projection matrix defined in Eq. (1), which, as shown in Refs. [47,70], depend on the position and orientation of the camera with respect to the global system of reference fixed to cylinder.

The perspective scale factor w_{v} depends both on the projection matrix $\mathbf{P}_{\mathrm{v}}$ and the position of the observed point $\mathbf{x}$. This makes the mapping in Eq. (3) non-linear in the Euclidean space and linear in the projective space [46]. Consequently, as shown schematically in Fig. 1b, an infinite number of points can be projected into a given image point, that is all the points in front of the camera that lie on the projection line joining the focal point of the camera optics and the image point in the photosensor of the camera. Overall, this projection is non-invertible unless, as shown Fig. 1b, the target point is observed from two viewpoints. As discussed above with the schemes shown in Fig. 4, the more view-points are available the more accurate will be the actual localisation of the dot position, which, in practice, rather than on a projection line, lies on a small volume defined by the intersections of the view-cones defined by the focus of the optics (vertex) and edges of the photosensor pixel lightened in each view.

In this work, rather than implementing classical time-domain triangulation of multi-view images [47], the frequency-domain triangulation presented in [62] is exploited, which is particularly suited for the derivation of vibration and sound radiation spectra. In this method, the image-based displacements taken from each view are Fourier transformed in the frequency-domain and then used to implement a frequency-domain triangulation that provides the spectra of the physical displacements of given points in the cylinder. The multi-view video acquisitions are taken in sequence using a common, pre-recorded, stationary white noise excitation exerted by the shaker. Indeed, a strong pre-requisite of the frequency triangulation is that the multi-view acquisitions are taken for a common stationary excitation time-history, which is characterized by a pre-recorded white noise process such that the classical signal processing tools can be employed to reconstruct FRFs for each measurement viewpoint (e.g. see Ref [73]). In this study, instead of implementing 3DPT, the image-based displacement FRFs were reconstructed with Lucas-Kanade DIC videogrammetry approach, which relies on the speckled film glued on the cylinder [74]. More specifically, the DIC has been used to reconstruct the displacements at the centre points of the mesh of $N = 62 \times 20 = 1240$ quadrilateral elements the cylinder has been divided into (see Figs. 1c, 6b). Here, it is important to underline that the DIC videogrammetry has not relied on the green dots painted on the film, but instead on the small black dots forming the speckled pattern. For simplicity, hereafter, the grid of 62×20 centre points will be referred to as the "centre points".

Gorjup *et. al.* [62] showed that, assuming time-harmonic vibrations, Eq. (3) can be rewritten in the following complex form

$$\mathbf{y}_{\mathrm{v}}(\omega) = \frac{1}{w_{\mathrm{v}}}\mathbf{P}_{\mathrm{v}}\mathbf{x}(\omega), \tag{4}$$

where the vectors $\mathbf{y}_{\mathrm{v}}(\omega)$, $\mathbf{x}(\omega)$ contain the complex coefficients of the Fourier transform of the time history of the position of the j-th point in the image 2D space and physical 3D space respectively. As for the classical time-domain formulation, Eq. (4) can be used to retrieve the position of the j-th point in the physical coordinates to within a scaling factor w_{v}. Hence, to derive the true position, triangulation should be implemented, that is the expression in Eq. (4) should be solved for the multiple view recordings. In this case, recalling that

$$\mathbf{y}_{\mathrm{vj}}(\omega) \times \frac{1}{w_{\mathrm{v}}}\mathbf{P}_{\mathrm{v}}\mathbf{x}_{\mathrm{j}}(\omega) = 0, \tag{5}$$

the following matrix expression can be established for the j-th point

$$\mathbf{A}_{\mathrm{j}}\mathbf{x}_{\mathrm{j}}(\omega) = 0, \tag{6}$$

where 0 is a $3\mathrm{V} \times 1$ vector of zeroes and $\boldsymbol{A}$ is the following $3\mathrm{V} \times 4$ matrix built using the skew-antisymmetric matrix operator $[\,]_{\times}$:

$$\mathbf{A}_{\mathrm{j}} = \begin{bmatrix} \left[\mathbf{y}_{1\mathrm{j}}\right]_{\times} & \mathbf{P}_1 \\ \vdots & \vdots \\ \left[\mathbf{y}_{\mathrm{Vj}}\right]_{\times} & \mathbf{P}_{\mathrm{V}} \end{bmatrix}. \tag{7}$$

Equation (6) forms a homogeneous system of 3 V linearly dependent equations in 2 V unknowns, which can be cast into a set of 2 V independent equations [47].

In practice, the image plane coordinates of the projected points are affected by digitalization errors, noise errors, etc. such that, the non-trivial solutions of the system of equations defined in (6) can be found only numerically with the Singular Value Decomposition (SVD) method [46]. The solutions are thus bound to be influenced by errors that arise from both the numerical calculations and the actual digitalization and noise errors that affect the coordinates of the centre points in the image plane of the camera for the 18 viewpoint acquisitions. Once the frequency-dependent complex positions have been reconstructed in the Euclidean space, the complex

amplitudes of the actual vibration displacements can be readily calculated as follows

$$\mathbf{d}_{\mathrm{j}}(\omega) = \mathbf{x}_{\mathrm{j}}(\omega) - \mathbf{x}_{\mathrm{j,ref}}. \tag{8}$$

Here the vector $\mathbf{x}_{\mathrm{j,ref}}$ defines the reference position of the j-th point in the physical coordinates. The radial component of the displacement can then be calculated by projecting the vector $\mathbf{d}_{\mathrm{j}}(\omega)$ in the radial direction defined by the unit vector $\mathbf{n}_j$:

$$w_j(\omega) = \mathbf{d}_{\mathrm{j}}(\omega) \cdot \mathbf{n}_j. \tag{9}$$

Finally, the dynamic flexibility FRF [75] giving the ratio between the complex amplitude of the radial displacement at the j-th centre point and the complex amplitude of the radial force applied to the cylinder can be derived straightforwardly as follows

$$\alpha_j(\omega) = \frac{w_j(\omega)}{f_r(\omega)}, \tag{10}$$

where $f_r(\omega)$ is the complex amplitude of the time-harmonic radial force acting on the cylinder, which, as done for the displacements, is derived from a Fourier transform of the force time history $f_r(t)$. As discussed above, in practice, the dynamic flexibilities are estimated with respect to stationary random processes. More specifically the optical measurements are taken for a white noise force excitation $f_r(t)$ and, according to classical signal processing theory (e.g. see ref. [73]), the dynamic flexibilities $\alpha_j(\omega)$ are estimated from the power and cross spectral density functions of the radial displacements and radial force. In this work the H_1 estimator was used, which is unbiased to the presence of output noise, that is noise arising from the camera acquisitions. Also, the classical measures that guarantee a proper reconstruction of the FRFs from discretized time histories were adopted (e.g. excitation filtering to avoid aliasing, FFT implementation, windowing, overlapping, averaging). In particular, the FRFs were generated by averaging 10 FRFs obtained from consecutive blocks of the displacement and force time-histories with 10% overlap. The accuracy of the measured FRFs was ensured with respect to the spectrum of the ordinary coherence function. The reader interested into the details of these aspects is on the one hand referred to classical Signal Processing textbooks focussed on FRFs estimation such as Ref. [73] and on the other hand to the work by Gorjup *et. al.* [62] that outlines in detail the frequency-domain triangulation approach.

3.2. Cylinder total flexural vibration

For stationary ergodic time-harmonic processes, the total flexural vibration of the cylinder can be conveniently derived in terms of the time-averaged total flexural kinetic energy,

$$\overline{K} = \lim_{T\to\infty} \frac{1}{\mathrm{T}} \int_0^T K(t)\mathrm{d}t, \tag{11}$$

where, for a thin-walled cylinder, the instantaneous total flexural kinetic energy is given by:

$$K(t) = \frac{1}{2}\rho_c h_c \int_{S_c} \dot{w}(\mathbf{x},t)^2 \mathrm{d}S_c. \tag{12}$$

Thus, for time-harmonic radial velocities characterised by complex amplitude $\dot{w}(\mathbf{x},\omega) = \mathrm{j}\omega w(\mathbf{x},\omega)$,

$$\overline{K}(\omega) = \frac{1}{4}\rho_c h_c \int_{S_c} |\dot{w}(\mathbf{x},\omega)|^2 \mathrm{d}S_c. \tag{13}$$

Here, ρ_c is the density of the material of the cylinder having thickness h_c and surface area $S_c = \pi D_c H_c$. This integral expression can be approximated by a Riemann mid-point sum over the regular mesh of $N = 62 \times 20 = 1240$ quadrilateral elements into which the surface of the cylinder was divided to, such that:

$$\overline{K}(\omega) \cong \frac{\rho_c h_c A_e}{4} \sum_{j=1}^{N} \left| \dot{w}_j(\omega) \right|^2, \tag{14}$$

where $\dot{w}_j(\omega)$ is the complex amplitude of the radial velocity at the centre of the j-th element and $A_e = S_c/N$ is the area of the quadrilateral elements the cylinder has been subdivided into (they all have the same area).

At this point, recalling the formulation presented above for the reconstruction from multi-view camera measurements of the complex amplitudes of the radial vibration displacements at the centres of the mesh of 62×20 quadrilateral elements, the time-averaged kinetic energy at the circular frequency ω can be expressed in terms of the dynamic flexibility defined in Eq. (10), such that

$$\overline{K}(\omega) \cong \omega^2 \frac{\rho_c h_c A_e}{4} \sum_{j=1}^{N} |\alpha_j(\omega)|^2 f_{r0}^2, \tag{15}$$

where $f_{r0} = |f_r(\omega)|$ is the amplitude of the radial force exerted by the shaker, which was kept to a constant value f_{r0} in the frequency

range of interest.

In practice, this summation is implemented with a vector formulation. To this end, the complex displacements and the dynamic flexibility FRFs are cast into the following column vectors $\mathbf{w}(\omega) = [\, w_1(\omega) \quad \cdots \quad w_N(\omega) \,]^{\mathrm{T}}$ and $\mathbf{a}(\omega) = [\, \alpha_1(\omega) \quad \cdots \quad \alpha_N(\omega) \,]^{\mathrm{T}}$, such that

$$\mathbf{w}(\omega) = \mathbf{a}(\omega) f_r(\omega). \tag{16}$$

Hence, recalling Eqs. (14), (15),

$$\overline{K}(\omega) \cong \omega^2 \frac{M_e}{4} \mathbf{w}^{\mathrm{H}}(\omega)\mathbf{w}(\omega), \tag{17}$$

that is

$$\overline{K}(\omega) \cong \omega^2 \frac{M_e}{4} \mathbf{a}^{\mathrm{H}}(\omega)\mathbf{a}(\omega) f_{r0}^2, \tag{18}$$

where $M_e = \rho_c h_c A_e$ is the mass of one quadrilateral element.

3.3. Cylinder total sound radiation

As seen for the vibrations, for stationary ergodic time-harmonic processes, the total sound radiation by the cylinder can be conveniently derived in terms of the time-averaged total sound power radiation,

$$\overline{P} = \lim_{T\to\infty} \frac{1}{\mathrm{T}} \int_0^T P(t)\mathrm{d}t, \tag{19}$$

where, as shown in Fig. 1d, the instantaneous total sound power radiation $P(t)$ of the baffled cylinder is obtained by integrating over a cylindrical surface S_{r} that encloses the baffled cylinder the sound intensity $\mathbf{I}(\mathbf{x}_{\mathrm{r}}, t) = p(\mathbf{x}_{\mathrm{r}}, t)\dot{\mathbf{u}}(\mathbf{x}_{\mathrm{r}}, t)$, which is given by the product of the sound pressure $p(\mathbf{x}_{\mathrm{r}}, t)$ and the particle velocity vector $\dot{\mathbf{u}}(\mathbf{x}_{\mathrm{r}}, t)$ at position $\mathbf{x}_{\mathrm{r}}$ over the surface S_{r}. In general, the particle velocity, and thus the sound intensity too, are characterised by three components. However, in practice, the integration is carried out over a large surface S_{r} where the radiated sound waves locally resemble plane waves. In this case the particle velocity is oriented in radial direction such that $\mathbf{I}(\mathbf{x}_{\mathrm{r}}, t) \cong I_{\mathrm{r}}(\mathbf{x}_{\mathrm{r}}, t) = p(\mathbf{x}_{\mathrm{r}}, t)\dot{u}_{\mathrm{r}}(\mathbf{x}_{\mathrm{r}}, t)$, where $I_{\mathrm{r}}(\mathbf{x}_{\mathrm{r}}, t)$ and $\dot{u}_{\mathrm{r}}(\mathbf{x}_{\mathrm{r}}, t)$ are the sound intensity and the particle velocity in radial direction. Hence, for a large cylindrical measurement surface S_{r} having a diameter considerably bigger than that of the cylinder, i.e. $D_{\mathrm{r}} \gg D_{\mathrm{c}}$, and significantly bigger than the acoustic wavelength, i.e. ,$D_{\mathrm{r}} \gg \lambda$, the instantaneous total sound power radiation is given by

$$P(t) = \int_{S_{\mathrm{r}}} I_{\mathrm{r}}(\mathbf{x}_{\mathrm{r}}, t)\mathrm{d}S_{\mathrm{r}} = \int_{S_{\mathrm{r}}} p(\mathbf{x}_{\mathrm{r}}, t)\dot{u}_{\mathrm{r}}(\mathbf{x}_{\mathrm{r}}, t)\mathrm{d}S_{\mathrm{r}}. \tag{20}$$

In this study a simpler approach is proposed, where, as depicted in Fig. 1c and d, the closed surface S_{r} is collapsed onto the surface of the radiating structure, that is on the surface of the flexible cylinder S_{c}. In this case, the fluid particle velocity over the surface of the radiating structure coincides with the radial, i.e. flexural, velocity of the cylinder, such that the instantaneous total sound power radiation can be derived from the following integral defined over the surface of the flexible cylinder only:

$$P(t) = \int_{S_{\mathrm{c}}} p(\mathbf{x}, t)\dot{w}(\mathbf{x}, t)\mathrm{d}S_{\mathrm{c}}. \tag{21}$$

Thus, considering time-harmonic sound pressure and radial velocity with complex amplitudes $p(\mathbf{x}, \omega)$ and $\dot{w}(\mathbf{x}, \omega) = j\omega w(\mathbf{x}, \omega)$, the time-averaged total sound power radiation results given by

$$\overline{P}(\omega) = \frac{1}{2} \int_{S_{\mathrm{c}}} \mathrm{Re}\{p^*(\mathbf{x}, \omega)\dot{w}(\mathbf{x}, \omega)\}\mathrm{d}S_{\mathrm{c}}, \tag{22}$$

where ()* is the complex-conjugate of the argument.

The integral in Eq. (22) requires the derivation of the sound pressure over the surface S_{c}. This can be accomplished analytically starting from the K-H integral [65–69], which, considering the whole surface $S = S_c \cup S_{b1} \cup S_{b2}$ of the flexible cylinder, S_c, and rigid baffles, S_{b1} and S_{b2}, states that the complex amplitude of the sound pressures $p(\mathbf{x}_{\mathrm{a}}, \omega)$ at position $\mathbf{x}_{\mathrm{a}}$ in the acoustic field is given by

$$p(\mathbf{x}_{\mathrm{a}}, \omega) = -\int_S \left(p(\mathbf{x}, \omega) \frac{\partial G(|\mathbf{x}_{\mathrm{a}} - \mathbf{x}|, \omega)}{\partial r} + j\omega\rho_0 G(|\mathbf{x}_{\mathrm{a}} - \mathbf{x}|, \omega)\dot{w}(\mathbf{x}, \omega) \right) dS. \tag{23}$$

Here, ρ_0 is the density of air and $G(|\mathbf{x}_{\mathrm{a}} - \mathbf{x}|, \omega)$ is a Green's function that satisfies the inhomogeneous Helmholtz acoustic equation and the condition of outward sound radiation into an unbounded acoustic domain, that is the Sommerfeld free radiation condition [65–69]. This integral equation is composed by two parts: the first, provides the sound radiation due to the scattering of sound on the walls of the

cylinder and baffles whereas, the second, provides the sound radiation generated by the flexural vibration of the flexible cylinder only. Recalling that $k = \omega/c$ is the acoustic wavenumber and c is the speed of sound, the simplest Green's function that satisfies these conditions is the so-called 1st-kind Green's function (or free-space Green's function) [65–69]:

$$g(|\mathbf{x}_a - \mathbf{x}|, \omega) = \frac{e^{-jk|\mathbf{x}_a - \mathbf{x}|}}{4\pi|\mathbf{x}_a - \mathbf{x}|}. \tag{24}$$

For the cylindrical radiator at hand, the adoption of this Green's function in the K-H integral would lead to a two steps calculus, where the sound pressure $p(\mathbf{x}, \omega)$ on the surface of the cylinder and baffles is first derived setting $\mathbf{x}_a = \mathbf{x}'$ in the integral and then the K-H integral is employed again to calculate the sound pressure $p(\mathbf{x}_a, \omega)$ in the acoustic field. However, as discussed in [66,69], there is another common form, called 2nd-kind Green's function, which satisfies Neumann boundary condition, that is $\partial G(|\mathbf{x}_a - \mathbf{x}|, \omega)/\partial r|_{r=R_c} = 0$, where R_c is the radius of the cylinder. In this case the first part of the K-H integral vanishes and the sound pressure can be calculated directly from Eq. (23) with a single step procedure considering only the surface of the vibrating cylinder:

$$p(\mathbf{x}_a, \omega) = -j\omega\rho_0 \int_{S_c} G(|\mathbf{x}_a - \mathbf{x}|, \omega)\dot{w}(\mathbf{x}, \omega)\mathrm{d}S_c. \tag{25}$$

The Neumann boundary condition imposes that the sound field generated by an infinitesimal vibrating element of the flexible cylinder $\mathrm{d}S_c$ satisfies rigid wall boundaries of the radiating object, that is of the flexible cylinder and two baffles in this specific case. Stepanishen [76], first derived the solution of the simplified K-H integral expression given in Eq. (25) for the sound radiation of a baffled cylinder. Here the following expression obtained in [77] is used instead, which, as assumed in this study, was derived for time-dependence $\exp(j\omega t)$:

$$p(r_a, \theta_a, z_a, \omega) = -j\frac{\omega\rho_0}{2\pi^2}\int_0^{2\pi}\int_0^{H_c}\left(\dot{w}(R_c, \theta, z, \omega)\sum\nolimits_{m=0}^{+\infty}\varepsilon_m \cos(m(\theta_a - \theta))\int_0^{\infty}\frac{\cos(k_z(z_a - z))}{k_r R_c}\frac{H_n^{(2)}(k_r r_a)}{H_n^{(2)'}(k_r R_c)}dk_z\right)R_c d\theta dz. \tag{26}$$

Here, $\varepsilon_m = 2$ for $m \neq 0$ whereas $\varepsilon_m = 1$ for $m = 0$. Also, $H_n^{(2)}, H_n^{(2)'}$ are the 2nd-kind Hankel function and its derivative respectively [72]. Moreover, $k_r = \sqrt{k^2 - k_z^2}$ where k_z is the projection of the acoustic wavenumber into longitudinal direction. As shown in [78], if $\exp(-j\omega t)$ where assumed, then Eq. (26) would have used 1st-kind Hankel function and therein derivative (i.e. $H_n^{(1)}$ and $H_n^{(1)'}$ [72]). Moreover, the term outside the integral would have been $+\omega\rho_0/(2\pi^2)$.

In the end, substituting Eq. (26) into Eq. (22), the time-averaged total sound power radiation results given by the following double integral

$$\overline{P}(\omega) = \frac{1}{2}\int_{S_c}\int_{S_c}\mathrm{Re}\{\dot{w}(\mathbf{x}', \omega)^* Z(\mathbf{x}'|\mathbf{x}'', \omega)\dot{w}(\mathbf{x}'', \omega)\}\mathrm{d}S_c\mathrm{d}S_c, \tag{27}$$

where, considering the complex amplitude of the volume velocity $\dot{U}_r(\mathbf{x}'', \omega) = \dot{w}(\mathbf{x}'', \omega)\mathrm{d}S_c$ produced by the radial vibration of the infinitesimal area of the cylinder $\mathrm{d}S_c$, the acoustic impedance $Z(\mathbf{x}'|\mathbf{x}'', \omega)$ results given by (see Refs. [67,79–81] for the numerous definitions of acoustic impedance given in books)

$$Z(\mathbf{x}'|\mathbf{x}'', \omega) = \frac{p(\mathbf{x}', \omega)}{\dot{U}_r(\mathbf{x}'', \omega)}. \tag{28}$$

Recalling Eq. (26), the acoustic impedance for the cylinder problem at hand results given by

$$Z(\mathbf{x}'|\mathbf{x}'', \omega) = -j\frac{\omega\rho_0}{2\pi^2}\sum\nolimits_{m=0}^{+\infty}\varepsilon_m \cos(m(\theta' - \theta''))\int_0^{\infty}\frac{\cos(k_z(z' - z''))}{k_r R_c}\frac{H_n^{(2)}(k_r R_c)}{H_n^{(2)'}(k_r R_c)}dk_z. \tag{29}$$

As seen for the kinetic energy, the integral expressions for the time-averaged total sound power radiation given in Eqs. (22) and (27) can be approximated by a Riemann mid-point sum over the mesh of $N = 62 \times 20 = 1240$ quadrilateral elements of the cylinder, such that

$$\overline{P}(\omega) = \frac{A_e}{2}\sum_{j=1}^{N}Re\left\{p_j^*(\omega)\dot{w}_j(\omega)\right\} = \frac{1}{2}\sum_{i=1}^{N}\sum_{j=1}^{N}\mathrm{Re}\left\{\dot{w}_i^*(\omega)Z_{ij}(\omega)\dot{w}_j(\omega)\right\}. \tag{30}$$

where $p_j(\omega)$ and $\dot{w}_j(\omega)$ are the complex amplitudes of the sound pressure and radial velocity at the centre of the j-th element and

$$Z_{ij}(\omega) = \frac{A_e p_i(\omega)}{\dot{w}_j(\omega)} = -j\frac{\omega\rho_0 A_e^2}{2\pi^2}\sum\nolimits_{m=0}^{+\infty}\varepsilon_m \cos(m(\theta_i - \theta_j))\int_0^{\infty}\frac{\cos(k_z(z_i - z_j))}{k_r R_c}\frac{H_n^{(2)}(k_r R_c)}{H_n^{(2)'}(k_r R_c)}dk_z \tag{31}$$

In this case too, the complex velocities at the centre points of the mesh of elements can be obtained from the dynamic flexibility relation of Eq. (10) such that

$$\overline{P}(\omega) = \frac{1}{2}\omega^2 \sum_{i=1}^{N}\sum_{j=1}^{N} \mathrm{Re}\{ f_r^*(\omega)\alpha_i^*(\omega) Z_{ij}(\omega)\alpha_j(\omega) f_r(\omega) \}, \tag{32}$$

where $f_r(\omega)$ is the complex amplitude of the radial force exerted by the shaker.

As done above, these summations can be implemented with algebraic expressions based on the vectors of the complex velocities $\dot{\mathbf{w}}(\omega) = \begin{bmatrix} \dot{w}_1(\omega) & \cdots & \dot{w}_N(\omega) \end{bmatrix}^{\mathrm{T}}$ and complex pressures $\mathbf{p}(\omega_k) = [\, p_1(\omega) \quad \cdots \quad p_N(\omega) \,]^{\mathrm{T}}$ at the grid of centres points and the vector $\mathbf{a}(\omega) = \lfloor\, \alpha_1(\omega) \quad \cdots \quad \alpha_N(\omega) \,\rfloor^{\mathrm{T}}$ with the dynamic flexibilities such that

$$\overline{P}(\omega) = \frac{A_e}{2}\mathrm{Re}\{ \mathbf{p}^{\mathrm{H}}(\omega)\dot{\mathbf{w}}(\omega) \} = \frac{1}{2}\mathrm{Re}\left\{ \dot{\mathbf{w}}^{\mathrm{H}}(\omega)\mathbf{Z}(\omega)\dot{\mathbf{w}}(\omega) \right\}, \tag{33}$$

where $()^{\mathrm{H}}$ is the Hermitian-transpose matrix operator and $\mathbf{Z}(\omega)$ is a square matrix with the acoustic impedances given in Eq. (31). Here, the $\mathbf{Z}(\omega)$ matrix is symmetric and thus the time average total sound power radiation can be expressed in the following compact matrix form (see Section 3.6.2 in Ref. [65]):

$$\overline{P}(\omega) = \dot{\mathbf{w}}^{\mathrm{H}}(\omega)\mathbf{R}(\omega)\dot{\mathbf{w}}(\omega), \tag{34}$$

which, recalling Eq. (16) with the matrix expression of the dynamic flexibilities obtained from the camera measurements, becomes

$$\overline{P}(\omega) = \omega^2 \mathbf{a}^{\mathrm{H}}(\omega)\mathbf{R}(\omega)\mathbf{a}(\omega) f_{r0}^2, \tag{35}$$

where $f_{r0} = |f_r(\omega)|$ is the amplitude of the radial force exerted by the shaker. Also, $\mathbf{R}(\omega)$ is the radiation matrix [65], whose elements are defined as follows:

$$R_{ij}(\omega) = \frac{1}{2}\mathrm{Re}\{ Z_{ij}(\omega) \} = \mathrm{Re}\left\{ -j\frac{\omega\rho_0 A_e^2}{4\pi^2} \sum\nolimits_{m=0}^{+\infty} \varepsilon_m \cos\big(m(\theta_i - \theta_j)\big) \int_0^{\infty} \frac{\cos\big(k_z(z_i - z_j)\big)}{k_r R_c} \frac{H_n^{(2)}(k_r R_c)}{H_n^{(2)'}(k_r R_c)} dk_z \right\}. \tag{36}$$

In the numerical calculations implemented in this study, the infinite summation $\sum_{m=0}^{+\infty}(\ )$ was truncated to the first $M+1$ terms that guarantee convergence. Also, it was noticed that when $k_z > k$, $k_r = \sqrt{k^2 - k_z^2}$ becomes imaginary, such that, according to Skudrzyk [72], the following equivalence was made:

$$\frac{1}{k_r R_c}\frac{H_n^{(2)}(k_r R_c)}{H_n^{(2)'}(k_r R_c)} = \frac{K_n(|k_r|R_c)}{|k_r|R_c K_n'(|k_r|R_c)}, \tag{37}$$

where K_n is the modified Bessel function of the second kind. For computing purposes, the integral $\int_0^{\infty}(\ )\mathrm{d}k_z$ in Eq. (36) was also approximated into a Riemann middle-point sum, such that

$$R_{ij}(\omega) \cong \mathrm{Re}\left\{ -j\frac{\omega\rho_0 A_e^2}{4\pi^2} \sum\nolimits_{m=0}^{M} \varepsilon_m \cos\big(m(\theta_i - \theta_j)\big) \sum_{r=0}^{R} \frac{\cos\big(r\Delta k_z(z_i - z_j)\big)}{\sqrt{k^2 - (r\Delta k_z)^2}\, R_c} \frac{H_n^{(2)}\left(\sqrt{k^2 - (r\Delta k_z)^2}\, R_c\right)}{H_n^{(2)'}\left(\sqrt{k^2 - (r\Delta k_z)^2}\, R_c\right)} \Delta k_z \right\}, \tag{38}$$

where Δk_z and R had been fixed in such a way as to guarantee convergence of the integral $\int_0^{\infty}(\ )\mathrm{d}k_z$.

For completeness, beside the proposed approach based on the integration of the sound intensity over the radiating surface (Fig. 1c), the total sound power radiation was also derived with the classical approach where the sound intensity is integrated over a large surface that encloses the radiating object. In this case, the cylindrical surface S_r shown in Fig. 1d. Thus, recalling Eq. (20) and considering the fact that, in the far-field, the sound waves locally resemble a plane wave over the measurement surface S_r such that the particle velocity has radial direction given by $\dot{u}_r(\mathbf{x}_r, t) = p(\mathbf{x}_r, t)/(\rho_0 c)$, the instantaneous total sound power radiation results

$$P(t) = \frac{1}{\rho_0 c}\int_{S_r} p(\mathbf{x}_r, t)^2 \mathrm{d}S_r. \tag{39}$$

Hence, assuming time-harmonic sound waves, the time-averaged total sound power radiation is given by

$$\overline{P}(\omega) = \frac{1}{2\rho_0 c}\int_{S_r} |p(\mathbf{x}_r,\omega)|^2 \mathrm{d}S_r, \tag{40}$$

where $p(\mathbf{x}_r,\omega)$ is the complex amplitude of the time-harmonic sound pressure at position $\mathbf{x}_r$ on the measurement surface S_r. In principle, the measurement surface should enclose the flexible cylinder and the rigid baffles, thus it should be a cylinder with large diameter D_r and infinite length. In this study, a cylinder with finite length H_r has been considered instead, which, nevertheless, covers the whole flexible cylinder and a portion of the baffles sufficient to detect the sound field radiated by the structure and scattered by the baffles. As done above for the integration over the sound radiation surface S_c in Eq. (27), the total sound power radiation can be expressed in terms of the following double integration

$$\overline{P}(\omega) \cong \frac{1}{2}\int_{S_r}\int_{S_c} \mathrm{Re}\{\dot{w}^*(\mathbf{x},\omega) Z^*(\mathbf{x}_r|\mathbf{x},\omega) Z(\mathbf{x}_r|\mathbf{x},\omega)\dot{w}(\mathbf{x},\omega)\}\mathrm{d}S_c \mathrm{d}S_r, \tag{41}$$

where, recalling Eqs. (26) and (28)

$$Z(\mathbf{x}_r|\mathbf{x},\omega) = -j\frac{\omega\rho_0}{2\pi^2}\sum_{m=0}^{+\infty}\varepsilon_m \cos(m(\theta_r-\theta))\int_0^{\infty}\frac{\cos(k_z(z_r-z))}{k_r R_c}\frac{H_n^{(2)}(k_r r_r)}{H_n^{(2)'}(k_r R_c)}dk_z. \tag{42}$$

Here, (r_r,θ_r,z_r) are the coordinates of the points on the surface S_r. As highlighted in the formula, in this case Eq. (41) provides an approximated result since a finite radiation surface S_r is considered rather than an infinitely long cylinder. As shown in Fig. 1d, to simplify the calculus, the integrals over the measurement surface S_r and the radiation surface S_c have been converted into Riemann mid-point sums across the meshes of $N_r = 6\times 8 = 48$ and $N = 62\times 20 = 1240$ elements respectively, such that

$$\overline{P}(\omega) \cong \frac{A_r}{2\rho_0 c}\sum_{j=1}^{N_r}\left|p_j(\omega)\right|^2 = \frac{1}{2\rho_0 c}\sum_{i=1}^{N}\sum_{j=1}^{N_r}\dot{w}_i^*(\omega) Z_{ij}(\omega)^* Z_{ij}(\omega)\dot{w}_i(\omega), \tag{43}$$

where $A_r = S_r/N_r$ is the area of the quadrilateral elements in the radiation surface (here too they all have the same value). Considering the derivation presented above for the impedance terms in Eqs. (31) and (38), the impedances in the equation above result given by

$$Z_{ij}(\omega) = \frac{A_r p_i(\omega)}{\dot{w}_j(\omega)} = -j\frac{\omega\rho_0 A_r A_e}{2\pi^2}\sum_{m=0}^{M}\varepsilon_m \cos\left(m\left(\theta_i-\theta_j\right)\right)\sum_{r=0}^{R}\frac{\cos\left(r\Delta k_z\left(z_i-z_j\right)\right)}{\sqrt{k^2-(r\Delta k_z)^2}R_c}\frac{H_n^{(2)}\left(\sqrt{k^2-(r\Delta k_z)^2}\,r_i\right)}{H_n^{(2)'}\left(\sqrt{k^2-(r\Delta k_z)^2}\,R_c\right)}\Delta k_z. \tag{44}$$

As seen above, the complex velocities at the centre points of the 62×20 mesh of elements in the cylinder surface can be obtained from the dynamic flexibilities in Eq. (10) derived from the camera measurements, such that

$$\overline{P}(\omega) \cong \frac{A_r}{2\rho_0 c}\sum_{i=1}^{N_r}|p_i(\omega)|^2 = \frac{\omega^2}{2\rho_0 c}\sum_{i=1}^{N}\sum_{j=1}^{N_r} f_r^*(\omega)\alpha_i^*(\omega) Z_{ij}(\omega)^* Z_{ij}(\omega)\alpha_j(\omega) f_r(\omega). \tag{45}$$

Here too, the double summation in Eq. (45) can be casted in a compact matrix expression with reference to vector in Eq. (16) of dynamic flexibilities obtained from the camera measurements, such that:

$$\overline{P}(\omega) \cong \omega^2 \mathbf{a}^{\mathrm{H}}(\omega)\mathbf{Z}^{\mathrm{H}}(\omega)\mathbf{Z}(\omega)\mathbf{a}(\omega) f_{r0}^2, \tag{46}$$

where the matrix $\mathbf{Z}(\omega)$ contains the impedances defined in Eq. (44).

3.4. Cylinder total flexural vibration and total sound radiation from laser and microphone array measurements

As discussed in Section 2.3 and shown in Fig. 6, the validity of the vibration and sound radiation measurement approach based on multi-view video recordings proposed in this article has been assessed with classical vibration (laser vibrometer) and sound radiation (anechoic room and microphones array) measurements. As depicted in Fig. 6a, the laser vibrometer has been used to measure mobility FRFs given by the ratios between the complex amplitudes of the velocities measured at the grid of centre points, $\dot{w}_j(\omega) = j\omega w_j(\omega)$, and the complex amplitude of the radial force exerted on the cylinder, $f_r(\omega)$:

$$Y_j(\omega) = \frac{\dot{w}_j(\omega)}{f_r(\omega)} = j\omega\alpha_j(\omega). \tag{47}$$

Hence, recalling Eq. (14), the time-averaged kinetic energy has been derived with the following formula

$$\overline{K}(\omega) \cong \frac{\rho_c h_c A_e}{4} \sum_{j=1}^{N} |Y_j(\omega)|^2 f_{r0}^2. \tag{48}$$

Here too, the complex velocity and the mobility FRFs casted into the following column vectors $\dot{\mathbf{w}}(\omega) = \begin{bmatrix} \dot{w}_1(\omega) & \cdots & \dot{w}_N(\omega) \end{bmatrix}^{\mathrm{T}}$ and $\mathbf{Y}(\omega) = [\, Y_1(\omega) \quad \cdots \quad Y_N(\omega) \,]^{\mathrm{T}}$ were used, such that

$$\dot{\mathbf{w}}(\omega) = \mathbf{Y}(\omega) f_r(\omega), \tag{49}$$

and

$$\overline{K}(\omega) \cong \frac{M_e}{4} \dot{\mathbf{w}}^{\mathrm{H}}(\omega) \dot{\mathbf{w}}(\omega) = \frac{M_e}{4} \mathbf{Y}^{\mathrm{H}}(\omega) \mathbf{Y}(\omega) f_{r0}^2. \tag{50}$$

As shown in Fig. 6b, the total sound power radiation has been measured in an anechoic room with a microphone array that has generated a total of 48 FRFs given by the ratios of the complex amplitudes of the sound pressures, $p_i(\omega)$, measured at the centers of the 6×8 quadrilateral elements the radiation surface has been divided into and the complex amplitude of the radial force exerted on the cylinder, $f_r(\omega)$:

$$H_i(\omega) = \frac{p_i(\omega)}{f_r(\omega)}. \tag{51}$$

Hence, the time-averaged total sound power radiation has been derived from Eq. (40) after the integration over the radiating surface has been substituted into a Riemann mid-point sum over the mesh of elements the surface has been divided into:

$$\overline{P}(\omega) \cong \frac{A_r}{2\rho_0 c} \sum_{i=1}^{N_r} |H_i(\omega)|^2 f_{r0}^2. \tag{52}$$

As done above, the sound pressure and the acoustic FRFs can be cast into the following column vectors $\mathbf{p}(\omega) = \lfloor\, p_1(\omega) \quad \cdots \quad p_N(\omega) \,\rfloor^{\mathrm{T}}$ and $\mathbf{H}(\omega) = \lfloor\, H_1(\omega) \quad \cdots \quad H_N(\omega) \,\rfloor^{\mathrm{T}}$, such that

$$\mathbf{p}(\omega) = \mathbf{H}(\omega) f_r(\omega). \tag{53}$$

Thus, the time-averaged total sound power radiation results given by the following matrix relations

$$\overline{P}(\omega) \cong \frac{A_r}{2\rho_0 c} \mathbf{p}^{\mathrm{H}}(\omega) \mathbf{p}(\omega) = \frac{A_r}{2\rho_0 c} \mathbf{H}^{\mathrm{H}}(\omega) \mathbf{H}(\omega) f_{r0}^2. \tag{54}$$

4. Narrow and third-octave band spectra of K and P

The spectral analysis for the total flexural vibration and total sound radiation is here introduced with respect to narrow band and third-octave band spectra of the time-averaged total flexural kinetic energy (e.g. Eqs. (18), (50)) and the time-averaged total sound power radiation (e.g. Eqs. (35), (46), (54)). The third-octave band spectra were derived from the following relations for the n-th band [15]:

$$\mathrm{KEL}_n = 10 \log_{10} \frac{\overline{K}_n}{K_r}, \tag{55}$$

$$\mathrm{PWL}_n = 10 \log_{10} \frac{\overline{P}_n}{P_r} \tag{56}$$

where $K_r = 10^{-12}\mathrm{J} = 1\mathrm{pJ}$ and $P_r = 10^{-12}\mathrm{W} = 1\,\mathrm{pW}$ are reference values for the kinetic energy and sound power and

$$\overline{K}_n = \frac{\Delta B_n}{N_i} \sum_{i=i_1}^{i_2} \overline{K}(\omega_i), \tag{57}$$

$$\overline{P}_n = \frac{\Delta B_n}{N_i} \sum_{i=i_1}^{i_2} \overline{P}(\omega_i), \tag{58}$$

are the band-limited values, which were calculated using the spectral values $\overline{K}(\omega_i)$, $\overline{P}(\omega_i)$ given respectively in Eqs. (18), (50) and Eqs. (35), (46), (54). Here ΔB_n is the width of the n-th third-octave band and $N_i = i_2 - i_1$, where i_1, i_2 are the indices of the frequency-samples at the lower and maximum frequency of the third-octave band [2].

4.1. Spectra of K

To start with, Figs. 7 and 8 present the narrow and third-octave band spectra of the total vibration kinetic energy. The blue lines or bars show the reference spectra derived from the measurements taken with the laser vibrometer whereas the red lines or bars show the spectra obtained from the camera measurements and the formulations presented in Section 3. The narrow band spectra in Fig. 7 are characterised by a rich content of resonance peaks due to the low order flexural natural modes of the cylinder. In general, the two spectra overlap quite well, although the resonance peaks in the spectrum derived from the camera measurements are less pronounced than those in the spectrum derived from the laser vibrometer measurements. This is principally because the spectrum from the camera measurements has been derived with a coarser frequency sampling rate.

Fig. 8 shows that there is a reasonably good agreement between the third-octave band spectra derived from the camera video acquisitions (red bars) and from direct measurements taken with the laser vibrometer (blue bar) with differences of the two spectra confined between 1 and 5 dB. Apart from the first two third-octave bands, the vibration levels reconstructed from the camera acquisitions are lower than those obtained from the measurements with the laser vibrometer. As noticed above, this is mainly caused by the fact that a coarser narrow band spectrum was reconstructed from the camera measurements, which is therefore characterized by smoother resonance peaks than the spectrum derived from the laser vibrometer measurements. The larger differences of 4, 5 dB found at 400, 630, 1250, and 1600 Hz are most likely due to the fact that the two measurements couldn't be performed simultaneously. Thus, it could be that the flexural response of the cylinder has undergone changes between one measurement and another, due for example to temperature variations. Moreover, while the camera measurements took about half an hour, those with the laser vibrometer lasted several hours. Thus, it is likely that during the long acquisitions with the laser vibrometer, the cylinder flexural response varied significantly under the effect of heating produced by the shaker placed inside the cylinder to generate the radial force excitation.

4.2. Spectra of P

The analysis of the narrow band and third-octave band spectra for the total sound power radiation is organised in two parts: the first, is focussed on spectra derived from the vibration measurements using the formulation based on the integration of the sound intensity over the surface of the cylinder, e.g. Eq. (35), whereas, the second, considers the spectra calculated from the vibration measurements with the classical formulation that integrates the sound radiation over a far-field measurement surface, e.g. Eq. (46). For completeness, in both analyses, the sound power radiation is calculated from both the camera vibration measurements and the laser vibrometer measurements. In the latter case, Eqs (35) and (46) are still used assuming that $\mathbf{a}(\omega) = \mathbf{Y}(\omega)/(j\omega)$, where $\mathbf{Y}(\omega) = [\, Y_1(\omega) \quad \cdots \quad Y_N(\omega) \,]^T$ is the vector with the mobility FRFs measured with the vibrometer.

Considering first the spectra derived from the vibration measurements using the formulation based on the integration of the sound intensity over the surface of the cylinder, e.g. Eq. (35), the red line in Fig. 9 shows the narrow-band spectrum obtained from the camera measurements whereas the blue line in Fig. 10 shows the narrow-band spectrum derived from the laser vibrometer measurements. The

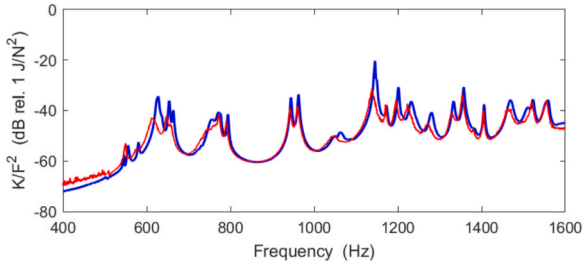

Fig. 7. Narrow band spectrum of the total vibration kinetic energy per unit force excitation from measurements with laser vibrometer (blue line) and camera (red line). (For interpretation of the references to colour in this figure legend, the reader is referred to the web version of this article.)

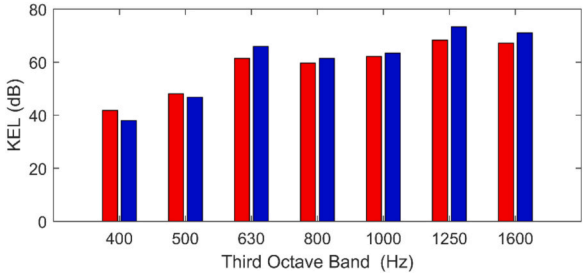

Fig. 8. Third-octave band spectrum of the total vibration kinetic energy from measurements with laser vibrometer (blue bar) and camera (red bar)–dB rel. to 10^{-12}J. (For interpretation of the references to colour in this figure legend, the reader is referred to the web version of this article.)

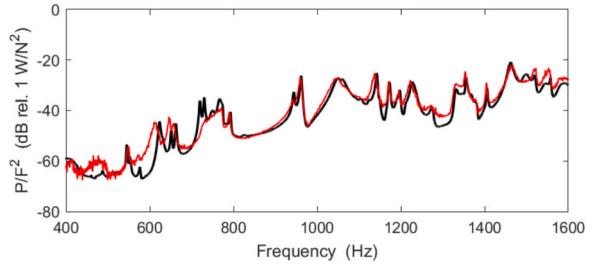

Fig. 9. Narrow band spectrum of the total sound power radiation per unit force excitation from measurements with microphones (black line) and calculated from measurements with camera (red line). (For interpretation of the references to colour in this figure legend, the reader is referred to the web version of this article.)

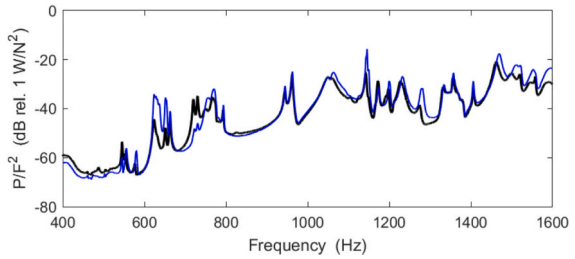

Fig. 10. Narrow band spectrum of the total sound power radiation per unit force excitation from measurements with microphones (black line) and calculated from measurements with laser vibrometer (blue line). (For interpretation of the references to colour in this figure legend, the reader is referred to the web version of this article.)

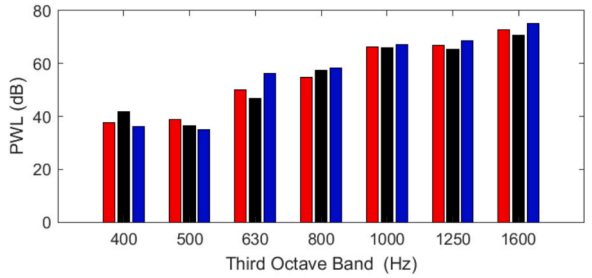

Fig. 11. Third-octave band spectrum of the total sound power radiation from measurements with microphones (black bars) and calculated from measurements with laser vibrometer (blue bars) and camera (red bars) – dB rel. to 10^{-12}W. (For interpretation of the references to colour in this figure legend, the reader is referred to the web version of this article.)

black line in both Figures shows the narrow-band spectrum reconstructed from the measurements in the anechoic room taken with the array of microphones using Eq. (54). In general, the spectra obtained from the camera and laser vibrometer measurements agree well with those obtained from the acoustic measurements. The spectrum produced from the camera measurements (red line in Fig. 9) shows some deviations compared to that derived from the acoustic measurements in the anechoic room (black line in Fig. 9), in particular between 600 and 750 Hz. Furthermore, it does not show deep troughs as those visible in the spectrum calculated from the acoustic measurements. These discrepancies are in any case limited and occur for sound power radiation values that, as will be seen below, have little influence on the third-octave values of the spectrum. The spectrum obtained from the laser vibrometer measurements (blue line in Fig. 10) also agree quite well with that obtained from the acoustic measurements in the anechoic room (black line in Fig. 10). It shows slightly more sharper resonance peaks, but, again, apart from the range 600 to 750 Hz, it generally overlaps reasonably well with the spectrum derived from acoustic measurements. Considering the three spectra in third-octave bands depicted in Fig. 11 (red bars from camera measurements, blue bars from laser measurements, black bars from microphone measurements), except for the third-octave band at 630 Hz, the differences between the third-octave levels obtained from the camera and laser vibration measurements and those obtained from the microphones acoustic measurements are rather small and limited between 1 and 2 dB.

Here, it should be highlighted that the acoustic-based measurement also offers an estimate, which, as a matter of facts, is based on a relatively small number of measurement points (the $N_r = 6 \times 8 = 48$ points depicted in Figs. 1d and 6b) and relies on the quality of the anechoic room, which may be affected by poor acoustic absorption at specific frequency bands as well as flanking noise effects (outdoor and indoor, including the equipment used for the measurement). On the contrary, the measurement approach proposed in this work relies on a rather dense grid of $N = 62 \times 20 = 1240$ vibration measurements, which in general is not affected by background

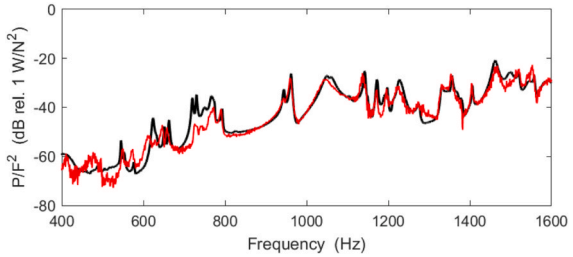

Fig. 12. Narrow band spectrum of the total sound power radiation per unit force excitation from measurements with microphones (black line) and reconstructed at microphones from measurements with camera (red line). (For interpretation of the references to colour in this figure legend, the reader is referred to the web version of this article.)

and flanking acoustic noise effects, unless they are so high to alter the vibration of the structure. In general, the camera vibration measurements are affected by pixelization errors, which principally depend on the time and spatial resolution of the camera. In this study a rather fast camera was employed, which guaranteed a correct reconstruction of the vibration field up to 2 kHz. The camera was also characterised by a rather high spatial resolution, which, as analysed in Section 4.1 above, ensured quite a reasonable reconstruction of the vibration field. Nevertheless, as discussed in Ref. [82], the errors arising from the pixelization of the displacements mostly have a random nature and thus, when the K-H integral formulation is implemented to derive the total sound power radiation, they tend to cancel out such that the accuracy of the sound radiation prediction results higher than that of the reconstructed vibration field. Hence, as seen in the previous section for the vibration spectra, the differences between the three spectra of the sound power radiation shown in Figs. 9 and 10, are most likely due to the fact that the three measurements were not performed simultaneously. Moreover, while the camera measurements took a relatively short time of the order of half an hour, the measurements with the laser vibrometer and array of microphone took a much longer time, in the order of several hours. Thus, it is quite possible that the flexural response of the cylinder underwent significant changes, particularly in the frequency range comprised between 600 and 750 Hz.

Considering now the spectra derived from the vibration measurements using the classical formulation that integrates the sound radiation over a far-field measurement surface, e.g. Eq. (46), the red line in Fig. 12 shows the narrow-band spectrum based on the camera measurements whereas the blue line in Fig. 13 shows the narrow-band spectrum obtained from the laser vibrometer measurements. Also, the black lines in both figures show the narrow-band spectrum derived from the measurements in the anechoic room taken with the array of microphones using Eq. (54). In this case, at low frequencies below about 800 Hz, compared to spectra from vibration measurements shown in Figs. 9 and 10, the spectra obtained from vibration measurements in Figs. 12 and 13 agree less well

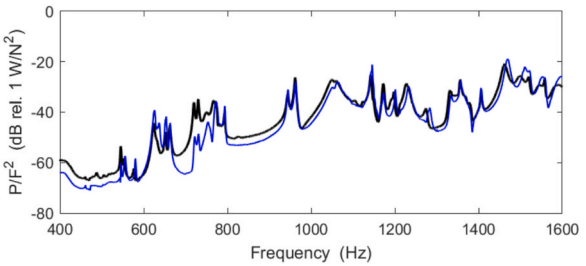

Fig. 13. Narrow band spectrum of the total sound power radiation per unit force excitation from measurements with microphones (black line) and reconstructed at microphones from measurements with laser vibrometer (blue line). (For interpretation of the references to colour in this figure legend, the reader is referred to the web version of this article.)

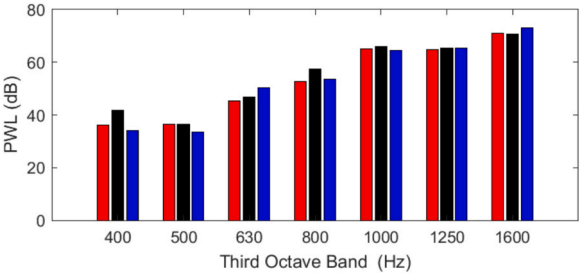

Fig. 14. Third-octave band spectrum of the total sound power radiation from measurements with microphones (black bars) and reconstructed at microphones from measurements with laser vibrometer (blue bars) and camera (red bars) – dB rel. to 10^{-12}W. (For interpretation of the references to colour in this figure legend, the reader is referred to the web version of this article.)

with that obtained from the acoustic measurement. This suggests that the derivation of the total sound power radiation from the integral of the sound intensity over the surface of the cylinder, e.g. using Eq. (35), is more accurate than the classical approach based on the integration of the sound radiation over a far-field measurement surface, e.g. using Eq. (46). As anticipated above, this is mainly due to the fact that in Eq. (35) the integration has been approximated by a Riemann mid-point sum over a smaller surface (e.g. $S_c \ll S_r$) with a much larger number of points (e.g. $N \gg N_r$), hence considering much smaller elemental areas $A_e \ll A_r$. Moreover, in this specific case, the integration in Eq. (46) has been implemented over a cylinder of finite length whereas, in principle it should have been an infinitely long cylinder. This is confirmed by the three spectra in third-octave bands depicted in Fig. 14 (red bars from camera measurements, blue bars from laser measurements, black bars from microphone measurements).

5. Extension to structures with uneven geometries

The methodology presented in this article for the measurement with optical cameras of the narrow band and third-octave band spectra of the total sound power radiated by a baffled cylindrical shell can be extended quite straightforwardly to structures and bodies with uneven geometries too. Indeed, overall, the time-averaged total sound power radiation of generic 2D or 3D structures can be derived with Eq. (33) using the vibrations reconstructed from multi-view camera acquisitions. There is just one critical issue that should be addressed for structures with arbitrary geometries: the calculation of the self and cross acoustic impedance terms. In fact, for radiators having uneven geometries, the Kirchhoff-Helmholtz integral in Eq. (23) cannot be solved analytically in closed form. Hence, approximate methods should be employed to reconstruct the acoustic field on the radiating surface necessary for the derivation of the self and cross impedance terms in Eq. (33) [65]. In general, both the acoustic Boundary Element Method and the acoustic Finite Element Method can be employed for this purpose. As shown schematically in Fig. 15 for a generic enclosure, the BEM method relies on the discretisation of the radiating surface with a mesh of planar elements (normally triangular or quadrilateral elements). Instead, the FEM approach utilises a mesh of solid elements for the whole sound field (normally hexahedral, pentahedral, tetrahedral elements), which, for sound radiation into free field, is delimited by the so-called "infinite elements" that enforce the unbounded sound radiation. In general, the BEM method provides a set of equations in the unknown sound pressures at the nodal points of the 2D mesh of elements with reference to the imposed transverse velocities at the same nodal points, which, for time-harmonic vibrations, can be written in the following matrix form:

$$\mathbf{Ap}(\omega) = j\omega\rho_0\mathbf{B}\dot{\mathbf{w}}(\omega). \tag{59}$$

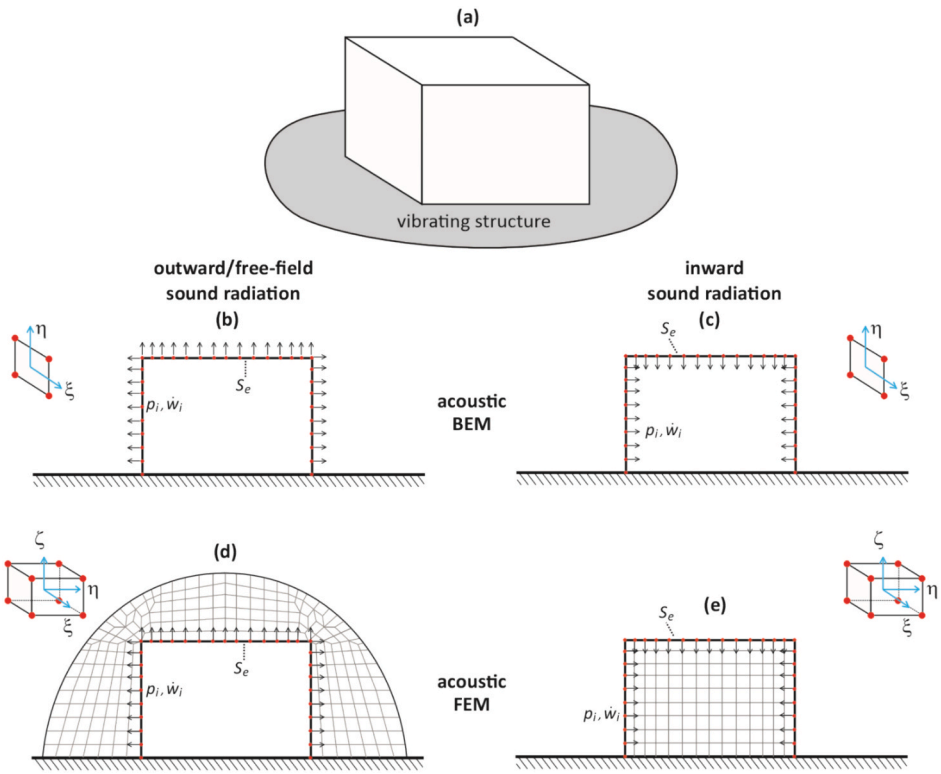

Fig. 15. BEM (b,c) and FEM (d,e) models for the derivation of the outward/free-field (left-hand side) and inward (right-hand side) total sound power radiation of a vibrating structure sitting on a rigid floor (a) based on the flexural vibrations reconstructed from the camera measurements (arrows) at the relevant nodal points of the BEM and FEM meshes highlighted by red dots. (For interpretation of the references to colour in this figure legend, the reader is referred to the web version of this article.)

Here the vectors $\mathbf{p}(\omega)$ and $\dot{\mathbf{w}}(\omega)$ contain the complex sound pressures and transverse velocities at the nodal points of the mesh. Also, the matrices **A** and **B** are derived by discretisation of the Kirchhoff-Helmholtz integral over the mesh of elements as described in Ref. [65] for example. Instead, the FEM approach provides a set of equations in the unknown sound pressure at the nodal points of the 3D mesh of elements in the radiation field with reference to the imposed volume velocities at the nodal points lying on the surface of the radiator, which for time harmonic vibrations, can be casted into the following matrix expression

$$\left[-\omega^2\mathbf{Q}+\mathrm{j}\omega\mathbf{D}+\mathbf{H}\right]\mathbf{p}(\omega)=\mathbf{V}\dot{\mathbf{w}}(\omega). \tag{60}$$

Here the vector $\mathbf{p}(\omega)$ contains the complex sound pressures on the nodes of the whole mesh of elements whereas the vector $\dot{\mathbf{w}}(\omega)$ contains the imposed complex velocities at the nodes of the mesh lying on the radiation surface. Also, the matrices **Q**, **D**, **H**, are global acoustic inertia, damping and stiffness matrices, which, as shown in Ref. [65], can be derived from discretisation of Hamilton's integral equation over the radiation volume covered by the mesh. Finally, the matrix **V** transforms the nodal velocities into volume velocity sources.

Both approaches can thus be used to derive the complex sound pressures $p_{\mathrm{i}}(\omega)$ at the nodal points laying on the surface of the structure due to the vibration velocities $\dot{w}_{\mathrm{i}}(\omega)$ at the same points reconstructed from multi-view camera acquisitions as described in Section 3.1 above. The self- and cross-impedance functions in Eq. (33), can then be calculated starting from Eq. (22), which can be split into a summation of integrals over the areas of the 2D BEM or 3D FEM elements lying on the radiation surface:

$$\overline{P}(\omega)=\frac{1}{2}\int_{S_s}\mathrm{Re}\{p^*(\mathbf{x},\omega)\dot{w}(\mathbf{x},\omega)\}\mathrm{d}S_{\mathrm{s}}=\frac{1}{2}\sum_{e=1}^{N_e}\int_{S_{\mathrm{e}}}\mathrm{Re}\{p^*(\mathbf{z},\omega)\dot{w}(\mathbf{z},\omega)\}\mathrm{d}S_{\mathrm{e}}. \tag{61}$$

Here S_{s} is the area of the whole structure whereas S_{e} is the area of the e-th BEM or FEM element laying on the vibrating surface of the structure. It is important to emphasize that, for the FEM elements laying on the radiating surface, the integration is implemented only over the face sitting on the surface of the radiator. Also, $p(\mathbf{z},\omega)$ and $\dot{w}(\mathbf{z},\omega)$ are the complex amplitudes of the sound pressure and particle velocity within the *e*-th element, which are formulated with respect to their nodal values assembled in column vectors $\mathbf{p}_{\mathrm{e}}(\omega)$ and $\dot{\mathbf{w}}_{\mathrm{e}}(\omega)$ respectively:

$$p(\mathbf{z},\omega)=\mathbf{b}(\mathbf{z})\mathbf{p}_{\mathrm{e}}(\omega), \tag{62}$$

$$\dot{w}(\mathbf{z},\omega)=\mathbf{b}(\mathbf{z})\dot{\mathbf{w}}_{\mathrm{e}}(\omega). \tag{63}$$

Here, the positions are defined with respect to local coordinates $\mathbf{z}=(\xi,\eta)$ and $\mathbf{z}=(\xi,\eta,\zeta)$ of the BEM and FEM elements respectively. Also, the row vector $\mathbf{b}(\mathbf{z})$ contains polynomial functions in ξ,η and ξ,η,ζ respectively (see Ref. [65] for more details). Substitution of Eqs. (62), (63) into Eq. (61) gives

$$\overline{P}(\omega)=\frac{1}{2}\sum_{e=1}^{N_e}\mathrm{Re}\left\{\mathbf{p}_e^H(\omega)\mathbf{C}_{\mathrm{e}}\dot{\mathbf{w}}_{\mathrm{e}}(\omega)\right\}, \tag{64}$$

where the matrix

$$\mathbf{C}_{\mathrm{e}}=\int_{S_{\mathrm{e}}}\mathbf{b}^{\mathrm{T}}(\mathbf{z})\mathbf{b}(\mathbf{z})\mathrm{d}S_{\mathrm{e}} \tag{65}$$

is derived either for the BEM elements laying on the radiating surface or for the FEM elements having one side facing the radiating surface. As noted above, for the FEM element the integration is carried out only for the face sitting on the surface of the radiator. Since the nodal pressures and velocities in either BEM or FEM formulations are gathered into global column vectors, $\mathbf{p}(\omega)$ $\dot{\mathbf{w}}(\omega)$, Eq. (64) can be rewritten in matrix form

$$\overline{P}(\omega)=\frac{1}{2}\mathrm{Re}\{\mathbf{p}^{\mathrm{H}}(\omega)\mathbf{C}\dot{\mathbf{w}}(\omega)\}, \tag{66}$$

where the matrix **C** is built by assembling the elements of the $\mathbf{C}_{\mathrm{e}}$ matrices in the appropriate row/column positions. The BEM and FEM Eqs. (59) and (60) can be used to derive impedance matrix relations between the sound pressure and vibration velocities at the nodal points

$$\mathbf{p}(\omega)=\mathbf{Z}_{\mathrm{n}}(\omega)\dot{\mathbf{w}}(\omega), \tag{67}$$

where the impedance matrix $\mathbf{Z}_{\mathrm{n}}(\omega)$ is given by

$$\mathbf{Z}_{\mathrm{n}}(\omega)=j\omega\rho_0\mathbf{A}^{-1}\mathbf{B}, \tag{68}$$

$$\mathbf{Z}_{\mathrm{n}}(\omega)=\left[-\omega^2\mathbf{Q}+\mathrm{j}\omega\mathbf{D}+\mathbf{H}\right]^{-1}\mathbf{V}, \tag{69}$$

respectively for the BEM and FEM formulations. Hence

$$\overline{P}(\omega) = \frac{1}{2}\mathrm{Re}\left\{\dot{\mathbf{w}}^{\mathrm{H}}(\omega)\mathbf{Z}(\omega)\dot{\mathbf{w}}(\omega)\right\}, \tag{70}$$

where $\mathbf{Z}(\omega) = \mathbf{Z}_{\mathrm{n}}^{\mathrm{H}}(\omega)\mathbf{C}$. In case the impedance matrix $\mathbf{Z}(\omega)$ were symmetric, then Eq. (70) could be rewritten with respect to a radiation matrix $\mathbf{R}(\omega) = 1/2\mathrm{Re}\{\mathbf{Z}(\omega)\} = 1/2\mathrm{Re}\left\{\mathbf{Z}_{\mathrm{n}}^{\mathrm{H}}(\omega)\mathbf{C}\right\}$, such that

$$\overline{P}(\omega) = \dot{\mathbf{w}}^{H}(\omega)\mathbf{R}(\omega)\dot{\mathbf{w}}(\omega). \tag{71}$$

As outlined at the beginning of Section 3.3. and discussed in books (e.g. see Refs. [1,2]) and international guidelines (e.g. see ISO Refs. [3,4]), in practice the total sound power radiation into free-field is generally derived by integrating the far-field sound intensity over a closed surface (normally a sphere, hemisphere, cylinder, rectangular-hexahedron). In this case, Eq. (20) should be used, which, assuming that the acoustic waves locally resemble plane waves and assuming time harmonic vibrations and sound radiation, leads to Eq. (40). As normally done for practical measurements with microphones in anechoic rooms (e.g. see Ref. [13]), the integral in Eq. (40) can be approximated by a summation of the sound pressure over a finite number of points regularly scattered over the measurement surface to give Eq. (43). In this case the BEM and FEM formulations can be employed to derive the transfer impedance functions between the vibration velocities reconstructed from the multi-view camera acquisitions at the nodal points of the BEM and FEM meshes laying on the surface of the radiator and the sound pressures at the nodal points of the BEM and FEM meshes sitting on the far-field closed surface. As a result, the time averaged total sound power radiation is calculated

$$\overline{P}(\omega) = \frac{S_{ef}}{2\rho_0 c}\dot{\mathbf{w}}^{H}(\omega)\mathbf{Z}_{\mathrm{r}}^{\mathrm{H}}(\omega)\mathbf{Z}_{\mathrm{r}}(\omega)\dot{\mathbf{w}}(\omega), \tag{72}$$

where the matrix $\mathbf{Z}_{\mathrm{r}}(\omega)$ contains these transfer impedance functions and $S_{ef} = S_r/N_r$ and N_r is the number of points on the radiation far-field surface S_r considered for the estimate of the total sound power radiation. Normally, the type of measurement surface and the number and positions of these points is chosen according to ISO guidelines (e.g. see Ref. [13]). Although this is a well-established measurement approach, since the multi-view camera acquisitions allows the full-field derivation of a flexural vibration of the structure over a dense grid of points, the method based on the derivation of Eq. (21) over the area of the radiator described above is preferred since it does not require the calculation of the transfer impedance matrix $\mathbf{Z}_{\mathrm{r}}(\omega)$. Moreover, it can be employed both for exterior free-field and interior sound radiation problems. The implementation of the formulation proposed in this section is thus recommended since it provides a direct estimate of the radiated sound power over a dense grid of nodal points without the need of extra calculations and, rather importantly, it can be used for both exterior and interior radiation problems of enclosures.

Indeed, as shown in Fig. 15, the approach proposed in this article can be employed to derive the spectra of both outward free-field and inward total sound power radiation, where, in the latter case, the camera measurements should be performed within the enclosure. Thus, it is expected that this methodology can be conveniently employed to assess the outward sound radiation of machine housings (e.g. of domestic appliances, of sections/components of road vehicles, etc.) as well as the inward sound transmission into enclosures (e.g. by trim panels of aircraft, by windows or walls of buildings, etc.). In particular, it can be suitably used to isolate the sound radiation of a specific portion of the radiating structure or machinery. Moreover, it can be effectively combined with emerging techniques where the excitation field is synthesized artificially with array of loudspeakers or shakers that reproduce specific vibro-acoustic fields such as: a) the pressure field exerted by a turbulent air flow on the flexible fuselage of aircraft, b) the diffuse acoustic field exerted on windows of building, c) the stochastic vibrations exerted by the road profile on tires of vehicles, d) the broadband stochastic vibrations exerted on payloads of satellite launch vehicles.

The formulation presented in this article is based on the derivation of dynamic flexibility FRFs $\alpha_j(\omega)$, which rely on the measurement of the force excitation exerted on the structure. Nevertheless, for practical applications where the vibration of the structure is not generated artificially with a shaker, the reference vibration signal can be measured directly onto the structure with an accelerometer sensor for example. Moreover, as normally done for vibro-acoustic measurements of real case structures subject to stationary disturbances, the spectra of the time-averaged total flexural kinetic energy and total sound power radiation can be derived directly from the power and cross-power spectral densities of the vibrations reconstructed from the camera acquisitions using Eq. (17) and Eq. (34) respectively (as an example, see Section 3.1 in Ref. [83]).

Although this article has outlined the general formulation for the derivation of the total sound power radiation, there are still a few challenges that need to be overcome to make this technology a viable solution for practical measurements of the sound radiation spectra of flexible structures. The first concerns the hardware: cameras with very high spatial and temporal resolution are mandatory to perform high frequency measurements, which typically should reach quite a few kHz (ideally up to 20 kHz) and should detect very small vibrations, particularly at the higher frequencies. In this respect, it should be emphasized that ordinary cameras provide information on positions, which are then used to reconstruct displacements. Thus, it would be helpful if new photosensor technologies were developed, which provide information on displacements such that vibration velocities can be reconstructed directly. A new class of cameras based on neuromorphic sensors, known as Event Cameras, has recently been developed [84–87], which indeed detect variations of brightness that would provide direct information on displacements. This is a rather appealing working principle since an elementary ± 1 binary information is generated by each pixel of the photosensor when there is a local change of brightness $\pm\Delta$. Hence, these cameras generate asynchronous flows of information on changes of brightness, which can be conveniently used to reconstruct displacements, although the tracking of target points of the structure from flows of events is not so straightforward. Nevertheless, they

generate flows of elementary information at unprecedented rates that can be handled with lower computing power compared to the data generated by classical photosensors that may prove instrumental to achieve broadband vibration measurements [88–92]. The implementation of multi-view acquisitions with multiple synchronized cameras or with single cameras where either the camera or the sample are displaced in between acquisitions also requires further development work, particularly to develop simple setups that can be installed, calibrated, synchronized with simple operations.

In parallel to the hardware, also the software side of this measurement approach presents a few challenges yet to be addressed. Firstly, at present the 3DPT or DIC image techniques still require the application on the radiating surface of markers or films with speckle patterns, which is not an easy task to perform and may alter the dynamic response of the structure too. Also, it would be important if the camera(s) could be used to acquire multi-view images of the radiator and radiating scene to then reconstruct a digital twin of their geometry that can be used to generate automatically the BEM and FEM meshes for the calculation of the radiation matrix. Finally, the reconstruction of the sound radiation due to practical disturbances for which no reference signal may be available should be addressed starting from the classical signal processing tools employed for direct acoustic measurements.

6. Conclusions

This research introduced and proved the feasibility of classical narrow band and third-octave band spectral measurements of the total vibration kinetic energy and total sound power radiation by a flexible cylinder connected to rigid baffles using optical camera video acquisitions. Two formulations have been proposed where the total radiated sound power has been derived by integration of the sound intensity over the radiating surface itself and over a far-field monitor surface where the sound waves resemble plane waves. Both the narrow-band and the third-octave-band vibration and sound radiation spectra reconstructed from the camera measurements overlap quite well with those derived from direct measurements taken respectively with a laser vibrometer and an array of microphones arranged according to ISO standards. The vibration spectrum reconstructed from the camera measurements replicates fairly well that obtained from direct measurements made by the laser vibrometer, although it has more rounded resonance peaks because it was calculated with a coarser sampling frequency. As a result, the third-octave band spectrum generated from the camera measurements is generally 1 to 5 dB lower than that obtained from the laser vibrometer measurements. The sound radiation spectrum obtained from the camera measurements replicates rather well that obtained from direct acoustic measurements in the anechoic room. There is just a critical band comprised between 600 and 750 Hz where the sound level predicted from the camera measurements shows marked differences from that measured in the anechoic room with microphones. Nevertheless, the deviations between the third-octave band spectrum derived from the camera measurements and that derived from direct acoustic measurements in the anechoic room are confined between 1 and 2 dB only. The study has shown that the derivation of the total sound power radiation based on the integration of sound intensity over the radiating surface is generally more accurate than that based on the integration of the sound intensity over a closed far field surface.

CRediT authorship contribution statement

Paolo Gardonio: Writing – review & editing, Writing – original draft, Investigation, Formal analysis, Conceptualization. **Sofia Baldini:** Writing – review & editing, Writing – original draft, Investigation, Formal analysis, Conceptualization. **Domen Gorjup:** Writing – review & editing, Writing – original draft, Investigation, Formal analysis, Conceptualization. **Janko Slavič:** Writing – review & editing, Writing – original draft, Investigation, Formal analysis, Conceptualization. **Roberto Rinaldo:** Writing – review & editing, Writing – original draft, Investigation, Formal analysis, Conceptualization.

Declaration of competing interest

The authors declare that they have no known competing financial interests or personal relationships that could have appeared to influence the work reported in this paper.

Acknowledgements

The authors would like to acknowledge the ESPERT project, which was supported by the University of Udine and the partial financial support from the Slovenian Research Agency, Slovenia (research core funding No. P2-0263).

Data availability

Data will be made available on request.

References

[1] R.F. Barron, Industrial noise control and acoustics, Dekker, 2003.
[2] D.A. Bies, C.H. Hansen, C.Q. Howard, K.L. Hansen, Engineering Noise Control, 6th Edition, CRC Press, 2024.
[3] ISO 3740:2019 Acoustics – Acoustics - Determination of sound power levels of noise sources – Guidelines for the use of basic standards.
[4] ISO 3744:2010 Acoustics – Determination of sound power levels and sound energy levels of noise sources using sound pressure – Engineering methods for an essentially free field over a reflecting plane.

[5] M.B. Salin, D.A. Kosteev, Nearfield acoustic holography-based methods for far field prediction, Appl. Acoust. 159 (2020) 107099, https://doi.org/10.1016/j.apacoust.2019.107099.
[6] L. Geng, X.-G. Chen, C.-D. He, W. Chen, S.-P. He, Compressive nonstationary near-field acoustic holography for reconstructing the instantaneous sound field, Mech. Syst. Signal Process. 204 (2023) 110779, https://doi.org/10.1016/j.ymssp.2023.110779.
[7] F. Fahy, Sound Intensity, 2nd ed. E & FN Spon, 1995.
[8] F. Jacobsen, H.-E. de Bree, A comparison of two different sound intensity measurement principles, J. Acoust. Soc. Am. 118 (2005) 1510–1517, https://doi.org/10.1121/1.1984860.
[9] J. Billingsley, R. Kinns, The acoustic telescope, J. Sound Vib. 48 (1976) 485–510, https://doi.org/10.1016/0022-460x(76)90552-6.
[10] R. Merino-Martínez, P. Sijtsma, M. Snellen, T. Ahlefeldt, J. Antoni, C.J. Bahr, D. Blacodon, D. Ernst, A. Finez, S. Funke, T.F. Geyer, S. Haxter, G. Herold, X.T. Huang, W.F. Humphreys, Q. Leclere, A.M.N. Malgoezar, U. Michel, T. Padois, A.V. Pereira, R. Gold, E. Sarradj, H. Siller, D.G. Simons, C. Spehr, A review of acoustic imaging methods using phased microphone arrays, 10 (2019) 197–230, https://doi.org/10.1007/s13272-019-00383-4.
[11] I.-J. Jung, J.-G. Ih, Design of a compact omnidirectional sound camera using the three-dimensional acoustic intensimetry, Mech. Syst. Signal Process. 172 (2022) 108970, https://doi.org/10.1016/j.ymssp.2022.108970.
[12] T. Padois, J. Fischer, C. Doolan, O. Doutres, Acoustic imaging with conventional frequency domain beamforming and generalized cross correlation: a comparison study, Appl. Acoust. 177 (2021), https://doi.org/10.1016/j.apacoust.2021.107914.
[13] ISO 3745:2012+A1:2017 Acoustics – Determination of sound power levels and sound energy levels of noise sources using sound pressure – Precision methods for anechoic rooms and hemi-anechoic rooms.
[14] ISO 3741:2010 Acoustics – Determination of sound power levels and sound energy levels of noise sources using sound pressure – Precision methods for reverberation test rooms.
[15] F.J. Fahy, Measurement of Audio-Frequency Sound in Air, in Fundamentals of Sound and Vibration, CRC Press Taylor & Francis Group, 2015.
[16] P. Gardonio, R. Rinaldo, R. Del Sal, L. Dal Bo, E. Turco, A. Fusiello, Multi-view videogrammetry for the estimate of plate sound radiation, in: Proceedings of the 14th Int. Conference on Vibration Measurements by Laser and Noncontact Techniques, 2021, https://doi.org/10.1088/1742-6596/2041/1/012013.
[17] P. Gardonio, R. Rinaldo, L. Dal Bo, R. Del Sal, E. Turco, A. Fusiello, Free-field sound radiation measurement with multiple synchronous cameras, Measurement 188 (2022), https://doi.org/10.1016/j.measurement.2021.110605.
[18] P. Gardonio, G. Guernieri, E. Turco, L. Dal Bo, R. Rinaldo, A. Fusiello, Reconstruction of the sound radiation field from flexural vibration measurements with multiple cameras, Mech. Syst. Signal Process. 195 (2023), https://doi.org/10.1016/j.ymssp.2023.110289.
[19] S. Baldini, G. Guernieri, D. Gorjup, P. Gardonio, J. Slavič, R. Rinaldo, 3D sound radiation reconstruction from camera measurements, Mech. Syst. Signal Process. 227 (2025), https://doi.org/10.1016/j.ymssp.2025.112400.
[20] T.C. Chu, W.F. Ranson, M.A. Sutton, Applications of digital-image-correlation techniques to experimental mechanics, Exp. Mech. 25 (3) (1985) 232–244, https://doi.org/10.1007/BF02325092.
[21] T. Ryall, C. Fraser, Determination of structural modes of vibration using digital photogrammetry, J. Aircraft 39 (1) (2002) 114(6).
[22] C. Warren, C. Niezrecki, P. Avitabile, Frf measurements and mode shapes determined using image-based 3D point-tracking, in: T. Proulx (Ed.), Modal Analysis Topics, vol. 3, Springer New York, New York, NY, 2011, pp. 243–252.
[23] S.W. Park, H.S. Park, J.H. Kim, H. Adeli, 3D displacement measurement model for health monitoring of structures using a motion capture system, Measurement 59 (2015) 352–362.
[24] J. Baqersad, C. Niezrecki, P. Avitabile, Full-field dynamic strain prediction on a wind turbine using displacements of optical targets measured by stereophotogrammetry, Mech. Syst. Signal Process. 62–63 (2015) 284–295, https://doi.org/10.1016/j.ymssp.2015.03.021.
[25] P. Poozesh, J. Baqersad, C. Niezrecki, P. Avitabile, E. Harvey, R. Yarala, Large-area photogrammetry based testing of wind turbine blades, Mech. Syst. Signal Process 86 (Part B) (2017) 98–115, https://doi.org/10.1016/j.ymssp.2016.07.021.
[26] J. Baqersad, P. Poozesh, C. Niezrecki, P. Avitabile, Photogrammetry and optical methods in structural dynamics – a review, Mech. Syst. Signal Process. 86 (2017) 17–34, https://doi.org/10.1016/j.ymssp.2016.02.011.
[27] R.S. Pappa, J.T. Black, J.R. Blandino, T.W. Jones, P.M. Danehy, A.A. Dorrington, Dot-projection photogrammetry and videogrammetry of gossamer space structures, J Spacecr Rockets 40 (2003) 858–867, https://doi.org/10.2514/2.7047.
[28] P.L. Reu, T.J. Miller, The application of high-speed digital image correlation, J. Strain Anal. Eng. Des. 43 (2008) 673e688.
[29] M.N. Helfrick, C. Niezrecki, P. Avitabile, T. Schmidt, 3D digital image correlation methods for full-field vibration measurement, Mech. Syst. Signal Process. 25 (2011) 917–927.
[30] P. Reu, Introduction to digital image correlation: best practices and applications, Exp. Tech. 36 (2012) 3–4.
[31] C. Nonis, C. Niezrecki, T.-Y. Yu, S. Ahmed, C.-F. Su, T. Schmidt, Structural health monitoring of bridges using digital image correlation, Health Monit. Struct. Biol, Syst, 2013.
[32] J. Baqersad, C. Niezrecki, P. Avitabile, Full-field dynamic strain prediction on a wind turbine using displacements of optical targets measured by stereo photogrammetry, Mech. Syst. Signal Process. 62 (2015) 284–295.
[33] P. Neri, A. Paoli, A.V. Razionale, C. Santus, Low-speed cameras system for 3D-DIC vibration measurements in the kHz range, Mech. Syst. Signal Process. 162 (2022), https://doi.org/10.1016/j.ymssp.2021.108040.
[34] D. Mastrodicasa, E. Di Lorenzo, S. Manzato, B. Peeters, P. Guillaume, 3D-DIC full field experimental modal analysis of a demo airplane by using low-speed cameras and a reconstruction approach, Mech. Syst. Signal Process. 227 (2025), https://doi.org/10.1016/j.ymssp.2025.112387.
[35] Y. Kato, S. Watahiki, M. Otaka, Full-field measurements of high-frequency micro-vibration under operational conditions using sub-Nyquist-rate 3D-DIC and compressed sensing with order analysis, Mech. Syst. Signal Process. 224 (2025), https://doi.org/10.1016/j.ymssp.2024.112179.
[36] D. Botto, S. Occhipinti, C.M. Firrone, P. Neri, High-frequency nonlinear vibration analysis through low-frequency stereo-camera systems, Mech. Syst. Signal Process. 223 (2025), https://doi.org/10.1016/j.ymssp.2024.111821.
[37] M. Pastor-Cintas, L. Felipe-Sesé, Á.J. Molina-Viedma, E. López-Alba, F.A. Díaz, Evaluation of 3D optical techniques for modal analysis during climatic test inside environmental chamber, Measurement 229 (2024), https://doi.org/10.1016/j.measurement.2024.114403.
[38] K. Luo, X. Kong, J. Li, J. Hu, L. Deng, Motion magnification for video-based vibration measurement of civil structures: a review, Mech. Syst. Signal Process. 220 (2024), https://doi.org/10.1016/j.ymssp.2024.111681.
[39] Z. Luo, B. Merainani, V. Baltazart, Q. Zhang, M. Döhler, Subpixel motion estimation for video-based target-free vibration monitoring under complex environmental conditions, Mech. Syst. Signal Process. 226 (2025), https://doi.org/10.1016/j.ymssp.2025.112342.
[40] X. Xiong, L. Liu, C. Wei, Sichao Tan, Mengmeng Dang, Zhi Zhong, Bin Liu, Lei Yu, Mingguang Shan,Visual vibration measurement using intensity optical flow with optical field correction under uneven illumination, Mechanical Systems and Signal Processing, Volume 240, (2025) 113431, https://doi.org/10.1016/j.ymssp.2025.113431.
[41] J. Luo, Q. Yang, S.-S. Law, G. Liu, An adaptive phase feedback algorithm for displacement tracking from video frames, Mech. Syst. Signal Process. 241 (2025) 113521, https://doi.org/10.1016/j.ymssp.2025.113521.
[42] Q. Leclère, H. André, J. Antoni, A. Burel, C. Capdessus, M. Cocconcelli, G. D'Elia, A.P. Daga, J.-L. Dion, M. El Badaoui, A. El Hidali, L. Garibaldi, F. Girardin, J. Griffaton, K. Gryllias, Y. Han, J. Helsen, F. Karkafi, K. Kestel, L. Kordylas, D. Kunte, S. Lo Feudo, A. Marsick, D. Marx, A.R. Mauricio, J. Miranda-Fuentes, C. Peeters, T. Poupon, D. Rémond, F. Renaud, J. Roussel, J. Touzet, T. Verwimp, L. Viale, M. Yazdanianasr, R. Zhu, Video-based diagnosis of a rolling element bearing using a high-speed camera, in: Feedback on the Survishno 2023 Conference Contest, Mechanical Systems and Signal Processing Volume 230, 2025, https://doi.org/10.1016/j.ymssp.2025.112601.
[43] T.J. Beberniss, D.A. Ehrhardt, High-speed 3d digital image correlation vibration measurement: recent advancements and noted limitations, Mech. Syst. Signal Process. 86 (2017) 35–48, https://doi.org/10.1016/j.ymssp.2016.04.014.
[44] R. Berke, C. Sebastian, R. Chona, E. Patterson, J. Lambros, High temperature vibratory response of hastelloy-x: Stereo-dic measurements and image decomposition analysis, Exp. Mech. 56 (2) (2016) 231–243, https://doi.org/10.1007/s11340-015-0092-3.

[45] P.L. Reu, D.P. Rohe, L.D. Jacobs, Comparison of dic and ldv for practical vibration and modal measurements, Mech. Syst. Signal Process. 86 (2017) 2–16, https://doi.org/10.1016/j.ymssp.2016.02.006.
[46] R. Hartley, A. Zisserman, Multiple view geometry in computer vision, Cambridge University Press, 2017.
[47] R. Del Sal, L. Dal Bo, E. Turco, A. Fusiello, A. Zanarini, R. Rinaldo, P. Gardonio, Structural vibration measurement with multiple synchronous cameras, Mech. Syst. Signal Process. 157 (2021) 107742, https://doi.org/10.1016/j.ymssp.2021.107742.
[48] P. Sturm, S. Maybank, On plane-based camera calibration: A general algorithm, singularities, applications, in: Proceedings. 1999 IEEE Computer Society Conference on Computer Vision and Pattern Recognition (Cat. No PR00149), Vol. 1, 1999, pp. 432–437. https://doi.org/10.1109/CVPR.199 9.786974.
[49] Z. Zhang, A flexible new technique for camera calibration, IEEE Trans. Pattern Anal. Mach. Intell. 22 (11) (2000) 1330–1334, https://doi.org/10.1109/34.888718.
[50] H.W. Kuhn, The hungarian method for the assignment problem, Naval Res. Logist. Quart. 2 (1–2) (1955) 83–97, https://doi.org/10.1002/nav.3800020109.
[51] L. Yu, B. Pan, Single-camera high-speed stereo-digital image correlation for full-field vibration measurement, Mech. Syst. Signal Process. 94 (2017) 374–383, https://doi.org/10.1016/j.ymssp.2017.03.008.
[52] J. Javh, J. Slavič, M. Boltežar, Measuring full-field displacement spectral components using photographs taken with a DSLR camera via an analogue Fourier integral, Mech. Syst. Signal Process. 100 (2018) 17–27, https://doi.org/10.1016/j.ymssp.2017.07.024.
[53] Y. Ming, et al., A novel low frequency vibration measurement method based on single camera, J. Phys. Conf. Ser. IOP Pub. (2018) 222016.
[54] B. Pan, L. Yu, Q. Zhang, Review of single-camera stereo-digital image correlation techniques for full-field 3D shape and deformation measurement, Sci. China Technol. Sci. 61 (2018) 2–20, https://doi.org/10.1007/s11431-017-9090-x.
[55] S. Barone, et al., Low-frame-rate single camera system for 3D full-field high-frequency vibration measurements, Mech. Syst. Signal Process. 123 (2019) 143–152.
[56] D. Gorjup, J. Slavič, A. Babnik, M. Boltežar, Still-camera multiview Spectral Optical Flow Imaging for 3D operating-deflection-shape identification, Mech. Syst. Signal Process. 152 (2021), https://doi.org/10.1016/j.ymssp.2020.107456.
[57] P. Etchepareborda, M.H. Moulet, M. Melon, Random laser speckle pattern projection for non-contact vibration measurements using a single high-speed camera, Mech. Syst. Signal Process. 158 (2021) 107719.
[58] F. Renaud, S. Lo Feudo, J.-L. Dion, A. Goeller, 3D vibrations reconstruction with only one camera, Mechanical Systems and Signal Processing, Volume 162 (2022), 108032, https://doi.org/10.1016/j.ymssp.2021.108032.
[59] Y. Wang, W. Hu, J. Teng, Y. Xia, Full-field displacement measurement of long-span bridges using one camera and robust self-adaptive complex pyramid, Mech. Syst. Signal Process. 215 (2024) 111451, https://doi.org/10.1016/j.ymssp.2024.111451.
[60] Z. Su, L. Wang, J. Zheng, J. Zhang, Multi-view camera motion compensation in bridge displacement measurement with panoramic camera, Mech. Syst. Signal Process. 231 (2025) 112717, https://doi.org/10.1016/j.ymssp.2025.112717.
[61] W. Zhu, Z. Cui, L. Chen, Z. Zhou, Xi Chu, S. Zhu, Robust monocular vision-based monitoring system for multi-target displacement measurement of bridges under complex backgrounds, Mechanical Systems and Signal Processing Volume 225 (2025) 112242, https://doi.org/10.1016/j.ymssp.2024.112242.
[62] D. Gorjup, J. Slavič, M. Boltežar, Frequency domain triangulation for full-field 3D operating-deflection-shape identification, Mech. Syst. Signal Process. 133 (2019) 106287, https://doi.org/10.1016/j.ymssp.2019.106287.
[63] J. Slavič, K. Zaletelj, D. Gorjup, D.P. Pasca, A. Aloisio, K.A. Kvåle, G.T. Frøseth, W. Weijtjens, A. Mujtaba, M. Česnik, A. Zorman, G. Tsialiamanis, I. Tomac, T. G. Ritto, D. Ocepek, D. Rohe, O.M. Silva, T.C.P. Masmeijer, K. Čufar, T. Bregar, M. Kodrič, A. El Mahmoudi, M. Pogačar, F. Trainotti, M. Göldeli, G. Čepon, R. Timbó, A.A. Cavallini, V.T. Costa, J.G.F. Santos, A.J. Hughes, J.G. Vargas, A. Fernandes, D.J. Rixen, K. Worden, M. Boltežar, Python open-source signal processing and modeling/simulation for scientific research in structural dynamics—A review, in: Mechanical Systems and Signal Processing Volume 241, 2025, https://doi.org/10.1016/j.ymssp.2025.113465.
[64] P. Gardonio, E. Turco, Tuning of vibration absorbers and Helmholtz resonators based on modal density/overlap parameters of distributed mechanical and acoustic systems, J. Sound Vib. 451 (2019) 32–70, https://doi.org/10.1016/j.jsv.2019.03.015.
[65] F.J. Fahy, P. Gardonio, Sound and Structural Vibration, Elsevier, 2007.
[66] M.C. Junger, D. Feit, Sound, structures, and their interaction, The Mit Press, Imp, 2010.
[67] A.D. Pierce, Acoustics, Acoustical Society of America through the American Institute of Physics, 1991.
[68] C. Lesuer, M. Gotteland, Rayonnement Acoustique. Éléments de base, in: Rayonnement Acoustique Des Structures, y C. Lesueur Editions Eyrolles, 1988: p. Ch 3.
[69] G.H. Koopmann, J.B. Fahnline, Designing quiet structures, A Sound power minimization approach. Academic Press, London, 1997.
[70] R. Hartley, A. Zisserman, Multiple View Geometry in Computer Vision, Cambridge University Press, Cambridge, 2004.
[71] F. Moreno-Noguer, V. Lepetit, P. Fua, Accurate Non-Iterative O(n) solution to the PnP Problem, in: 2007 IEEE 11th International Conference on Computer Vision, 2007, pp. 1–8, https://doi.org/10.1109/ICCV.2007.4409116.
[72] E. Skudrzyk, The Foundations of Acoustics, Springer-Verlag, New York, 1971.
[73] K. Shin, J.K. Hammond, Fundamentals of signal processing for sound and vibration engineers, John Wiley & Sons, Chichester, England; Hoboken, NJ, 2008.
[74] B. Lucas, T. Kanade, An Iterative image registration technique with an application to stereo vision, IJCAI (1981).
[75] P. Gardonio, M. Brennan. Mobility and impedance methods in structural dynamics. In Advanced applications in acoustics, noise and vibration, 1st Ed. Editors F. Fahy, J. Walker, Spon Press Press – Taylor & Francis Group 2004.
[76] P.R. Stepanishen, Radiated power and radiation loading of cylindrical surfaces with nonuniform velocity distributions, J. Acoust. Soc. Am. 63 (1978) 328–338, https://doi.org/10.1121/1.381743.
[77] C.B. Goates, C.B. Jones, S.D. Sommerfeldt, J.D. Blotter, Sound power of vibrating cylinders using the radiation resistance matrix and a laser vibrometer, J. Acoust. Soc. Am. 148 (2020) 3553–3561, https://doi.org/10.1121/10.0002870.
[78] Y. Sun, T. Yang, Y. Chen, Sound radiation modes of cylindrical surfaces and their application to vibro-acoustics analysis of cylindrical shells, J. Sound Vib. 424 (2018) 64–77, https://doi.org/10.1016/j.jsv.2018.03.004.
[79] L.E. Kinsler, A.R. Frey, A.B. Coppens, J.V. Sanders, Fundamentals of Acoustics, 4th Ed., John Wiley & Sons, Inc., Chichester, 2000.
[80] L.L. Beranek, T.J. Mellow, Acoustics, Sound Fields and Transducers, Academic Pres - Elsevier, Amsterdam, 2012.
[81] D. Thompson, P. Nelson. Fundamentals of Acoustics. In Fundamentals of Sound and Vibration, 2nd Ed. Editors F. Fahy and D. Thompson, CRC Press – Taylor & Francis Group 2015.
[82] P. Gardonio, R. Rinaldo, L. Dal Bo, R. Del Sal, E. Turco, A. Fusiello, Free-field sound radiation measurement with multiple synchronous cameras, Measurement 188 (2022) 110605, https://doi.org/10.1016/j.measurement.2021.110605.
[83] P. Gardonio, S. Miani, F. Blanchini, D. Casagrande, S.J. Elliott, Plate with decentralised velocity feedback loops: power absorption and kinetic energy considerations, J. Sound Vib. 331 (2012) 1722–1741.
[84] R. Benosman, C. Clercq, X. Lagorce, S.-H. Ieng, C. Bartolozzi, Event-based Visual Flow, IEEE Trans. Neural Netw. Learn. Syst. 25 (2014) 407–417.
[85] T. Delbruck, M. Lang, Robotic goalie with 3 ms reaction time at 4% CPU load using event-based dynamic vision sensor, Front. Neurosci. (2013).
[86] P. Purohit, R. Manohar, Field-programmable encoding for address-event representation, Front.in Neurosci. 16 (2022).
[87] G. Gallego, T. Delbrück, G. Orchard, C. Bartolozzi, B. Taba, A. Censi, S. Leutenegger, A.J. Davison, J. Conradt, K. Daniilidis, D. Scaramuzza, Event-based Vision: a Survey, IEEE Trans. Pattern Anal. Mach. Intell. 44 (2022) 154–180, https://doi.org/10.1109/TPAMI.2020.3008413.
[88] C. Dorn, S. Dasari, Y. Yang, C. Farrar, G. Kenyon, P. Welch, D. Mascareñas, Efficient full-field vibration measurements and operational modal analysis using neuromorphic event-based imaging, J. Eng. Mech. 144 (2018), https://doi.org/10.1061/(ASCE)EM.1943-7889.0001449.
[89] Z. Lai, I. Alzugaray, M. Chli, E. Chatzi, Full-field structural monitoring using event cameras and physics-informed sparse identification, Mech. Syst. Signal Process. 145 (2020) 106905, https://doi.org/10.1016/j.ymssp.2020.106905.

[90] C. Shi, N. Song, B. Wei, Y. Li, Y. Zhang, W. Li, J. Jin, Event-based Vibration Frequency Measurement with Laser-Assisted Illumination based on Mixture Gaussian distribution, IEEE Trans. Instrum. Meas. 72 (2023) 1–13, https://doi.org/10.1109/TIM.2023.3301911.
[91] M. Zhao, X. Shen, F. Jiang, in: Research on Mechanical Vibration Measurement Method Based on Event Camera, in, 2023, pp. 528–532, https://doi.org/10.1109/EEPS58791.2023.10257083.
[92] S. Baldini, F. Stazi, R. Bernardini, A. Fusiello, P. Gardonio, R. Rinaldo, Vibration measurement with neuromorphic vision sensors, Mech. Syst. Signal Process. (2026), https://doi.org/10.2139/ssrn.5638561.